

# Long-term in vitro corrosion behavior of Zn-3Ag and Zn-3Ag-0.5Mg alloys considered for biodegradable implant applications

Wątroba, Maria; Mech, Krzysztof; Bednarczyk, Wiktor; Kawałko, Jakub; Marciszko-Wiąckowska, Marianna; Marzec, Mateusz; Shepherd, Duncan E.T.; Bała, Piotr

DOI:

[10.1016/j.matdes.2021.110289](https://doi.org/10.1016/j.matdes.2021.110289)

License:

Creative Commons: Attribution (CC BY)

*Document Version*

Publisher's PDF, also known as Version of record

*Citation for published version (Harvard):*

Wątroba, M, Mech, K, Bednarczyk, W, Kawałko, J, Marciszko-Wiąckowska, M, Marzec, M, Shepherd, DET & Bała, P 2022, 'Long-term in vitro corrosion behavior of Zn-3Ag and Zn-3Ag-0.5Mg alloys considered for biodegradable implant applications', *Materials and Design*, vol. 213, 110289.  
<https://doi.org/10.1016/j.matdes.2021.110289>

[Link to publication on Research at Birmingham portal](#)

## General rights

Unless a licence is specified above, all rights (including copyright and moral rights) in this document are retained by the authors and/or the copyright holders. The express permission of the copyright holder must be obtained for any use of this material other than for purposes permitted by law.

- Users may freely distribute the URL that is used to identify this publication.
- Users may download and/or print one copy of the publication from the University of Birmingham research portal for the purpose of private study or non-commercial research.
- User may use extracts from the document in line with the concept of 'fair dealing' under the Copyright, Designs and Patents Act 1988 (?)
- Users may not further distribute the material nor use it for the purposes of commercial gain.

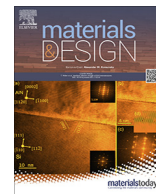
Where a licence is displayed above, please note the terms and conditions of the licence govern your use of this document.

When citing, please reference the published version.

## Take down policy

While the University of Birmingham exercises care and attention in making items available there are rare occasions when an item has been uploaded in error or has been deemed to be commercially or otherwise sensitive.

If you believe that this is the case for this document, please contact [UBIRA@lists.bham.ac.uk](mailto:UBIRA@lists.bham.ac.uk) providing details and we will remove access to the work immediately and investigate.



# Long-term *in vitro* corrosion behavior of Zn-3Ag and Zn-3Ag-0.5Mg alloys considered for biodegradable implant applications

Maria Wątroba<sup>a,\*</sup>, Krzysztof Mech<sup>b</sup>, Wiktor Bednarczyk<sup>a,c</sup>, Jakub Kawałko<sup>b</sup>, Marianna Marciszko-Wiackowska<sup>b</sup>, Mateusz Marzec<sup>b</sup>, Duncan E.T. Shepherd<sup>d</sup>, Piotr Bała<sup>a,b</sup>

<sup>a</sup> AGH University of Science and Technology, Faculty of Metals Engineering and Industrial Computer Science, Al. A. Mickiewicza 30, 30-059 Krakow, Poland

<sup>b</sup> AGH University of Science and Technology, Academic Centre for Materials and Nanotechnology, Al. A. Mickiewicza 30, 30-059 Krakow, Poland

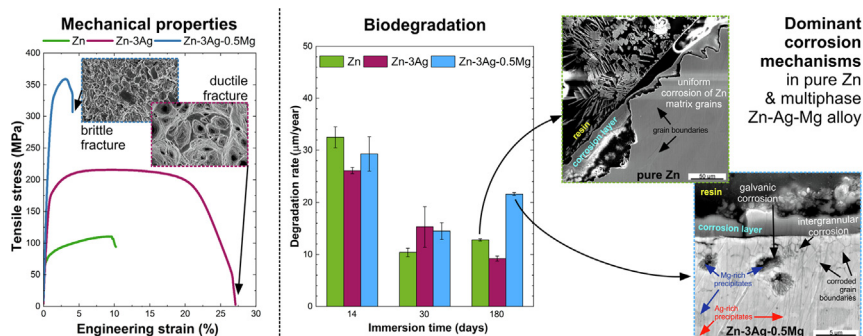
<sup>c</sup> Warsaw University of Technology, Faculty of Materials Science and Engineering, Wołoska 141, 02-507 Warsaw, Poland

<sup>d</sup> Department of Mechanical Engineering, University of Birmingham, Birmingham B15 2TT, UK

## HIGHLIGHTS

- Additions of Ag and Mg provided grain refinement and multiphase microstructure.
- Investigated Zn alloys degraded mainly via intergranular and micro galvanic corrosion.
- Refined Zn grains and evenly distributed small precipitates provided uniform corrosion.
- Precipitates of the  $\epsilon$ -Zn<sub>3</sub>Ag phase corroded slower than Zn and remained in the pits.
- The corrosion rate of the Zn-3Ag-0.5Mg alloy after 180-day immersion was 21.6  $\mu\text{m}/\text{year}$ .

## GRAPHICAL ABSTRACT



## ARTICLE INFO

### Article history:

Received 25 September 2021

Revised 19 November 2021

Accepted 26 November 2021

Available online 02 December 2021

### Keywords:

Zn alloys

Microstructure

Mechanical properties

Biodegradation

Galvanic corrosion

Electrochemical measurements

## ABSTRACT

In this paper, Zn-3Ag and Zn-3Ag-0.5Mg alloys were studied in terms of applicability as biodegradable implant materials. The performed tensile, compression and bending tests indicate a high strengthening effect induced by the Ag and Mg additions, additionally resulting in grain size refinement. It was shown that sustaining plastic strain during deformation depends on the applied stress causing asymmetric mechanical behavior of the tested Zn-based materials. Electrochemical measurements and immersion tests in Hanks' solution lasting up to 180 days revealed that Ag and Mg contribute to the change of the Zn matrix's open circuit potential and the formation of micro-galvanic cells between the Zn grains and precipitates. The fine-grained microstructure and evenly distributed small precipitates led to uniform corrosion occurring via pit formation on the corroded surface due to intergranular and micro-galvanic corrosion mechanisms. The corrosion rate of the Zn-3Ag-0.5Mg alloy after 180 days was almost twice that of pure Zn and the Zn-3Ag alloy.

© 2021 The Authors. Published by Elsevier Ltd. This is an open access article under the CC BY license (<http://creativecommons.org/licenses/by/4.0/>).

## 1. Introduction

Biodegradable implants have a significant advantage over conventional permanent ones, as they do not require further medical intervention for their removal. However, the interaction between the dissolving implant and environment of the human body should

\* Corresponding author.

E-mail address: [mwatroba@agh.edu.pl](mailto:mwatroba@agh.edu.pl) (M. Wątroba).

be carefully studied to inhibit toxic reactions. Physiological fluids interact with the metallic material, causing its progressive dissolution, with the formation of corrosion products that are metabolized or removed from around the implant, and finally excreted [1]. Therefore, the corrosion rate is the main factor used to distinguish biodegradable metals. The most widely considered metals are magnesium (Mg), iron (Fe), and zinc (Zn). The rapid corrosion of Mg, associated with the accumulation of corrosion products and extensive hydrogen gas evolution, may result in the sudden loss of mechanical support for the healing tissue. The use of Fe for biomedical applications is hindered as it exhibits slow degradation in physiological fluids and may result in the formation of problematic corrosion products [2]. The material that, in recent years, has become a competitor of both Mg and Fe is Zn, which degrades at a rate between the two metals [3–5].

The biodegradation behavior depends on many factors related to both the studied material and biodegradation environment. From the material point of view, chemical composition, mechanical properties (when considering materials susceptible to stress corrosion cracking), surface characteristics (topography, roughness, surface energy, hydrophilic/hydrophobic properties, work function, chemical and physical properties of passive layer) and microstructural features should be considered. In terms of environmental factors, the experimental conditions (*in vitro* or *in vivo*), corrosive environment complexity, measurement type (static or dynamic), immersion time and the composition of the physiological fluid can strongly affect biodegradation behavior [1,6–9]. Based on published results, the degradation rate of pure Zn varies in the range of 13–320  $\mu\text{m}/\text{year}$  tested *in vitro* in physiological solutions within 30 days [10]. Alloying additions, especially those forming precipitates, increase the corrosion rate compared to pure Zn. According to research conducted on binary Zn alloys vs pure Zn, corrosion rates ranged from  $\sim 14$  to 30  $\mu\text{m}/\text{year}$  compared to 14  $\mu\text{m}/\text{year}$  for pure Zn. An almost 10-times higher corrosion rate was recorded during *in vivo* tests (from 140 to 260  $\mu\text{m}/\text{year}$ ) compared to *in vitro* tests. However, an accelerated degradation of Zn alloys compared to pure Zn also being observed [11]. Regardless of the applied experimental conditions, usually the alloying additions have a similar effect on the tested corrosion rate of Zn alloys compared to pure Zn *in vitro* and *in vivo* [12]. However, as *in vivo* experiments can be costly, timely and require animal testing, it is beneficial to test novel Zn alloys using fast and easy electrochemical measurements and immersion tests in simulated physiological fluids. These techniques give a quick view on the influence of certain alloying elements and fabrication techniques (necessary for mechanical properties enhancement) on the corrosion behavior.

It has been recently shown that multiphase Zn alloys can successfully overcome the limitations of pure Zn, in terms of biomedical application requirements, which is characterized by low strength and brittleness [13,14]. The optimal combination of alloying elements and use of complex thermomechanical processing provide properties exceeding the mechanical requirements for short-term implant material [10,15,16]. The strengthening of the Zn alloy is controlled via grain refinement, a  $\eta$ -Zn based solid solution, and intermetallic phases [17]. In multiphase Zn alloys, there are several effects that can be distinguished. Firstly, the synergistic effect of low-content different solute elements may provide additional strength and enable reaching the required ductility. This is a more favorable effect than obtaining required strength by means of high volume fractions of secondary phases, since they may galvanically couple with the matrix [18]. Secondly, the simultaneous addition of two or more elements may mitigate the precipitation of secondary phases from the thermodynamically unstable supersaturated solid solution during natural aging or thermomechanical processes [19–21]. Thirdly, in solid solution

strengthened Ag-, Cu- and Mn- rich fine-grained ternary Zn alloys, Mg- and Li-rich precipitates strengthen grain boundaries, hindering grain boundary sliding or creep [22–25]. When tailoring the alloy's mechanical behavior, the main challenge is not to influence the biodegradation and biocompatibility of pure Zn. Therefore, the formation of harmful corrosion products upon Zn alloying must be considered and studied. In biodegradable multiphase alloys, attention should be paid to the formation of micro-galvanic cells between the matrix and precipitates that can induce a local corrosion. Depending on their electrochemical potential compared to the Zn matrix they can accelerate or slow down the corrosion process. Strong local corrosion at micro-galvanic cells can deteriorate the mechanical integrity of an implant, while corrosion products in the form of a stable layer might result in decreased corrosion rates. Therefore, lower volume fraction of secondary phases or their small size and uniform distribution within the microstructure is highly desirable [26].

This work focuses on the effect of Ag and Mg additions on the corrosion properties of pure Zn, while following the alloys' mechanical behavior. Long-term *in vitro* biodegradation evaluation (greater than 30 days) have not been studied in detail [10], therefore the present research is focused on the corrosion development after 180-day immersion in Hanks' solution to assess the feasibility of using Zn-based alloys for biomedical applications. Additionally, this work is the first to present *in vitro* studies on the long-term biodegradation of Zn-3Ag (wt. %) and Zn-3Ag-0.5Mg (wt. %) alloys. The Zn-Ag-Mg alloy system has already been demonstrated to show promising mechanical performance for load-bearing applications [27–29], especially when fabricated using a two-stage hot-cold plastic deformation process, followed by post-deformation and short-term annealing [30]. This study extends on the already reported mechanical properties [27,30] by showing the alloys' asymmetric mechanical behavior during tension, compression and three-point bending.

## 2. Experimental materials and procedures

### 2.1. Materials processing

Samples of pure Zn, Zn-3Ag, and Zn-3Ag-0.5Mg (wt. %) alloys were prepared using pure zinc (99.995 wt. %), silver (99.995 wt. %), and magnesium (99.95 wt. %). The ingots were fabricated by induction melting at 650 °C and gravity casting into steel molds. The as-cast Zn alloys were annealed at 350 °C for 4 h and subsequently subjected to indirect hot extrusion (HE) at 250 °C.

### 2.2. Microstructural characterization and mechanical tests

Microstructural characterization of the as-extruded samples was performed on longitudinal cross-sections prepared by standard metallographic preparation. A scanning electron microscope (SEM; Versa 3D; FEI), equipped with energy dispersive X-ray spectrometry (EDS; Ultim Max; Oxford Instruments) and electron back-scattered diffraction (EBSD; Symmetry S2; Oxford Instruments) detectors, was used for microstructural observations. The AZtec software (Oxford Instruments) was used to acquire EBSD data and collect energy-dispersive spectra for chemical quantitative microanalysis. The analyses were performed at 20 kV and 23 nA. The EBSD maps for pure Zn ( $1000 \times 1000 \mu\text{m}^2$ ) and the Zn-3Ag and Zn-3Ag-0.5Mg alloys ( $150 \times 150 \mu\text{m}^2$ ) were acquired using a step size of 1.5  $\mu\text{m}$  and 0.15  $\mu\text{m}$ , respectively. The average grain size, crystallographic orientation maps and texture were analyzed (according to ASTM E2627-13 standard) using the MTEX toolbox in MATLAB™. A single grain was defined as a set of at least 5 points with a misorientation angle between neighboring grains greater

than 15. For grain size evaluation, the diameter of equivalent circle was used.

Tensile (standard ASTM E8-21) and compression (standard ASTM E9-19) tests were performed up to 50 % of deformation at a strain rate of  $10^{-3}$  1/s by means of a universal testing machine (Instron 5966; Instron) using tenfold  $\phi$  3 mm tensile specimens and  $\phi$  4 mm  $\times$  6 mm cylindrical samples, respectively. Additionally, ductility tests were performed using three-point bending (standard ASTM E290-14) on a mechanical testing machine (Bose ElectroForce 3300; ElectroForce Systems Group). The diameter of the loading nose and supports was  $\phi$  6 mm and the span between the lower supports was 30 mm. Samples, with geometries of  $\phi$  4 mm  $\times$  70 mm, were loaded under displacement control mode at 0.2 mm/s to provide a similar strain rate as during tension and compression. Three samples of each material were taken for each mechanical test. Flow stress was determined at a strain equal 5 %.

### 2.3. Electrochemical measurements

Electrochemical tests were performed using a potentiostat (Bio-Logic SP-300; Bio-Logic Science Instruments) equipped with the EC-Lab software (Bio-Logic Science Instruments). A three-electrode electrochemical cell consisting of a platinum mesh counter electrode, saturated Ag/AgCl reference electrode, and the working electrodes being flat Zn-based samples with 1 cm<sup>2</sup> of electrochemically active surface area (ECSA) was immersed in Hanks' solution to simulate the ion concentration of blood plasma (Table 1). The pH value was  $7.4 \pm 0.1$  and a temperature of  $37.5 \pm 0.5$  °C was maintained using an IKA HRC 2 Control thermostat. The longitudinal cross-sections of the samples were prepared by grinding, polishing, ultrasonic cleaning in ethanol, and drying. All electrochemical measurements were carried out after 2 h immersion in Hanks' solution to stabilize the open circuit potential (OCP) and reach steady-state conditions. Potentiodynamic curves were recorded at a scan rate of 1 mV/s in the range of  $-200$  mV to 200 mV vs. the OCP. Afterwards, the standard Tafel extrapolation method was used to determine the corrosion potential ( $E_{\text{corr}}$ ) and corrosion current density ( $i_{\text{corr}}$ ). The corrosion rate (CR,  $\mu\text{m}/\text{year}$ ) of each Zn-based material was estimated according to the ASTM G102-89 standard and using the following equation:

$$CR = k \cdot \frac{i_{\text{corr}} \cdot EW}{\rho} \quad (1)$$

where:  $k$  - conversion factor ( $3.27 \cdot 10^6$  ( $\mu\text{m} \cdot \text{g})/(\text{A} \cdot \text{cm} \cdot \text{year})$ ),  $i_{\text{corr}}$  - corrosion current density ( $\mu\text{A}/\text{cm}^2$ ) determined using the Tafel extrapolation method,  $EW$  - dimensionless equivalent weight, and  $\rho$  - density ( $\text{g}/\text{cm}^3$ ) of the Zn-based materials. Electrochemical impedance spectroscopy (EIS) measurements were conducted in a frequency range of 100 kHz to 1 Hz with an amplitude of  $\pm 10$  mV. Representative curves for each material can be found in the Results section.

### 2.4. Static immersion test

Prior to immersion tests, the cylindrical samples were ultrasonically cleaned in ethanol, dried, and placed in Hanks' solution with the 1 cm<sup>2</sup>:25 ml of surface area to solution volume ratio. Tests

were conducted at  $37.5 \pm 0.5$  °C (standard ASTM G31-72) for three selected experimental time intervals: 14, 30, and 180 days. Every 3 days, the medium was replaced with a fresh one to maintain the initial pH value of  $7.4 \pm 0.1$ . After 14, 30, and 180 days the samples were removed from Hanks' solution, and prepared for SEM corrosion products morphology observations, by cleaning in water and ethanol, and drying. Finally, corrosion products were removed from the samples' surface (following standard ASTM G1-90), by chemical ultrasonic cleaning with a chromium trioxide-based solution in H<sub>2</sub>O (200 g/L of CrO<sub>3</sub>) for 2 min (to avoid removing any metallic Zn), followed by rinsing with water, ethanol, and drying. The degradation rate was calculated based on the measured weight loss of three samples according to the following Eq. (2):

$$C_R = \frac{K \cdot W}{A \cdot t \cdot \rho} \quad (2)$$

where  $K$  - constant ( $8.76 \cdot 10^7$  for corrosion rate unit of  $\mu\text{m}/\text{year}$ ),  $W$  - weight loss (g),  $A$  - surface (cm<sup>2</sup>),  $t$  - exposure period (h), and  $\rho$  - density ( $\text{g}/\text{cm}^3$ ).

### 2.5. Characterization of corrosion products layer

The morphology and chemical microanalysis of the corrosion products formed after immersion tests and of the degraded surfaces after corrosion product removal was performed using the SEM-EDS technique, to analyze the top layer of the corrosion products and the corroded cross-sections of the samples. Additionally, the corrosion products formed after 180 days were characterized by X-ray diffraction measurements using an X-ray diffractometer (XRD; Empyrean; Malvern Panalytical) with Cu-K $\alpha$  radiation ( $\lambda = 1.5406$  Å) at 40 kV and 40 mA, a scanning rate of 0.4°/min, and a step size of 0.02°. XRD references were taken from the ICSD database. X-ray photoelectron spectroscopy (XPS; PHI 5000 VersaProbe; ULVAC-PHI) was conducted using monochromatic Al K $\alpha$  (1486.6 eV) X-rays focused to a 100  $\mu\text{m}$  spot and scanned over an area of 400  $\times$  400  $\mu\text{m}^2$ . The photoelectron take-off angle was 45° and the pass energy in the analyzer was set to 117.50 eV (0.5 eV step) for survey scans and 46.95 eV (0.1 eV step) to obtain high energy resolution spectra for the C 1s, Zn 2p and Ca 2p regions. Dual beam charge compensation, with 7 eV Ar<sup>+</sup> ions and 1 eV electrons, was used to maintain a constant sample surface potential regardless of sample conductivity. All XPS spectra were charge-referenced to the unfunctionalized saturated carbon (C-C) C 1s peak at 285.0 eV. The operating pressure in the analytical chamber was  $<3 \times 10^{-9}$  mbar. Spectra deconvolution was carried out using the MultiPak software (PHI). Spectrum background was subtracted using the Shirley method.

### 2.6. Statistical analysis

All measured data were expressed as mean  $\pm$  standard deviation. The statistical analysis was performed by analysis of variance (ANOVA) and Bonferroni's test using the OriginPro software (OriginLab). The statistically significant difference between groups was classified using a p-value assumed at \* $p < 0.05$ , \*\* $p < 0.01$ , and \*\*\* $p < 0.001$ .

**Table 1**  
Ion concentrations of blood plasma and Hanks' solution [31].

Medium	Na <sup>+</sup>	K <sup>+</sup>	Ca <sup>2+</sup>	Mg <sup>2+</sup>	HCO <sub>3</sub> <sup>-</sup>	Cl <sup>-</sup>	HPO <sub>4</sub> <sup>2-</sup>	SO <sub>4</sub> <sup>2-</sup>	Amino acid	Glucose	Protein
	mmol/L								g/L		
Blood plasma	142.0	5.0	2.5	1.5	27.0	103.0	1.0	0.5	0.25–0.4	~1.1	63 – 80
Hanks' solution	141.8	5.4	1.3	0.8	4.2	144.8	0.8	0.8	–	1.0	–



### 3. Results

#### 3.1. Microstructure and mechanical properties

The microstructures of Zn and Zn-3Ag, Zn-3Ag-0.5Mg alloys after hot extrusion (HE) are presented in Fig. 1. After HE, the Zn-based matrix consisted of equiaxed grains. The white precipitates occurring in Zn-3Ag and Zn-3Ag-0.5Mg alloys (marked with red arrows in Fig. 1b, c) are the  $\epsilon$ -Zn<sub>3</sub>Ag phase, according to the Zn-Ag phase diagram [32] and previous studies [27] for a concentration of 3% Ag. The visible dark grains in the microstructure of the Zn-3Ag-0.5Mg alloy (marked with yellow arrows in Fig. 1c) are composed of nanometric-sized precipitates of Zn<sub>11</sub>Mg<sub>2</sub> and Zn<sub>2</sub>Mg phases enriched in Ag, as shown in our previous work [27]. Both Ag and Mg hindered grain growth during dynamic recrystallization that took place during HE. The average grain size decreased from  $106.6 \pm 49.8 \mu\text{m}$  for pure Zn to  $10.3 \pm 4.6 \mu\text{m}$  and  $6.7 \pm 2.9 \mu\text{m}$  for the Zn-3Ag and Zn-3Ag-0.5Mg alloys, respectively. A typical  $(1\ 0\ \bar{1}\ 0)$  fiber texture with almost all basal poles oriented perpendicularly to the extrusion direction (ED), occurred in all investigated samples, as a result of basal slip system activation during HE, common for hexagonal close-packed (HCP) metals [33].

Fig. 2a presents the stress-strain tensile curves of the extruded materials. It can be observed that Ag additions enabled increasing Zn-alloy strength and ductility compared to pure Zn. As shown in Fig. 2d, over threefold (172 MPa) and twofold (217 MPa) higher yield strength (YS) and ultimate tensile strength (UTS) were recorded for the Zn-3Ag alloy, respectively. Additionally, the alloy exhibited a ductile fracture mode at elongation over 20 %, which is confirmed by the fractographic image included in Fig. 2a, where

characteristic dimples separated by elongated sharp edges can be seen. Grain refinement and a high-volume fraction of secondary phases in the Zn-3Ag-0.5Mg alloy caused an increase in YS (287 MPa) and UTS (362 MPa), which exceed the required values for short-term implant (200 MPa and 300 MPa, respectively [34]). However, a deterioration in plasticity ( $\epsilon_F = 4.1\%$ ) was registered, associated with the formation of transgranular fractures at the cleavage planes visible in the fractogram embedded in Fig. 2a.

Compressive stress-strain and bending load-displacement curves are presented in Fig. 2b and c, respectively. The highest compressive strength (446 MPa) was recorded for the Zn-3Ag-0.5Mg alloy. Pure Zn samples fractured at approx. 3.7 mm of displacement, almost directly after reaching 75 MPa of maximum stress. The tests for Zn-3Ag and Zn-3Ag-0.5Mg alloys were stopped after reaching over 20 mm of displacement without cracking. This indicates high deflection under a complex deformation state and lack of brittle fracturing for both alloys. Flow stress calculated at 5 % of flexural strain increased from 58 MPa up to 113 MPa for the Zn-3Ag alloy and 190 MPa in the Zn-3Ag-0.5Mg alloy.

#### 3.2. Electrochemical properties

The OCP of the investigated materials was measured in reference to an Ag/AgCl electrode for materials immersed in Hanks' solution for 2 h. According to Fig. 3a, there is no significant variation in OCP values during the immersion time. An initial slight decrease in OCP indicates the dissolution of the naturally-formed film at the electrode's surface [35]. After about 1 h, the OCP of all samples reached stable values, demonstrating the following

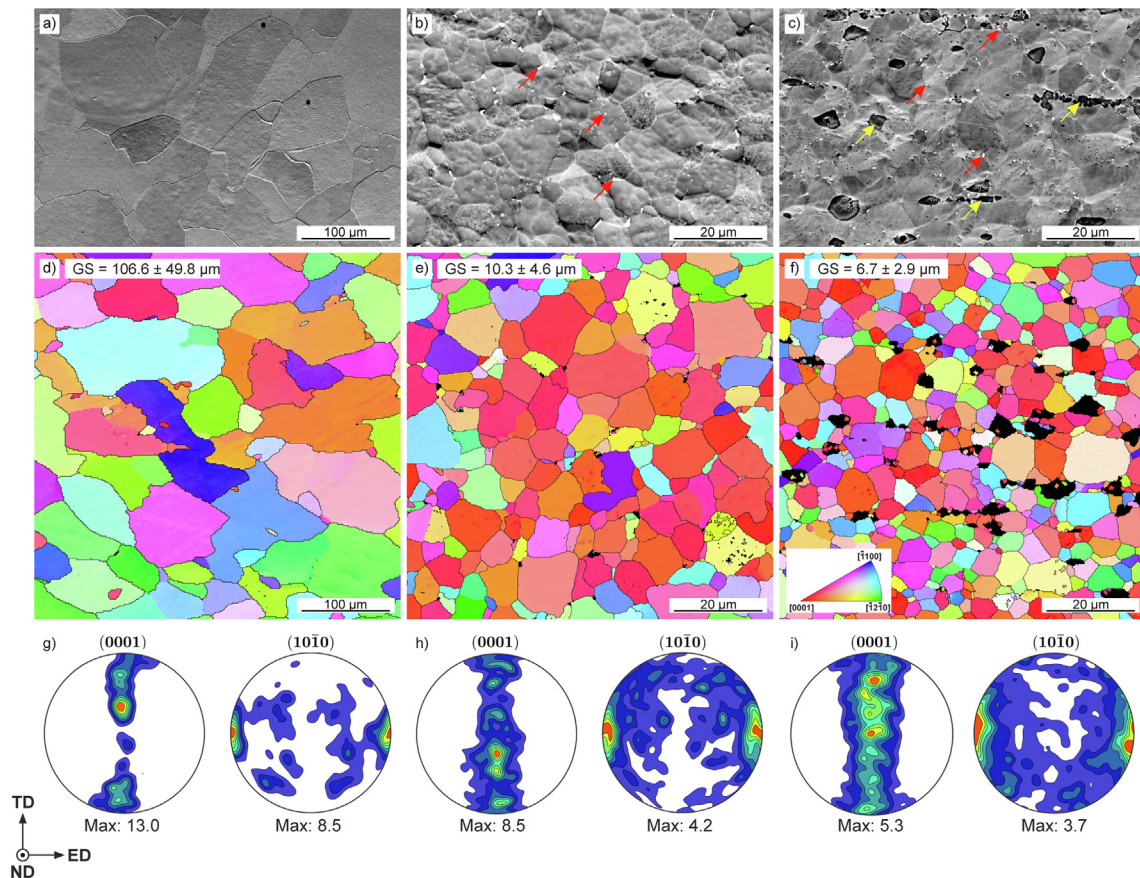


**Fig. 1.** Microstructures (a–c) and EBSD-IPF (Inverse Pole Figures) orientation maps (d–f), and  $(0\ 0\ 0\ 1)$  and  $(1\ 0\ \bar{1}\ 0)$  PF (Pole Figures) of HE pure Zn (a, d, g), Zn-3Ag (b, e, h), Zn-3Ag-0.5Mg (c, f, i) alloys in the longitudinal cross-sections. Note the different scale bars for Zn and Zn-based alloys. Red arrows (b, c) indicate Ag-rich precipitates, yellow arrows (c) indicate Mg-rich precipitates.

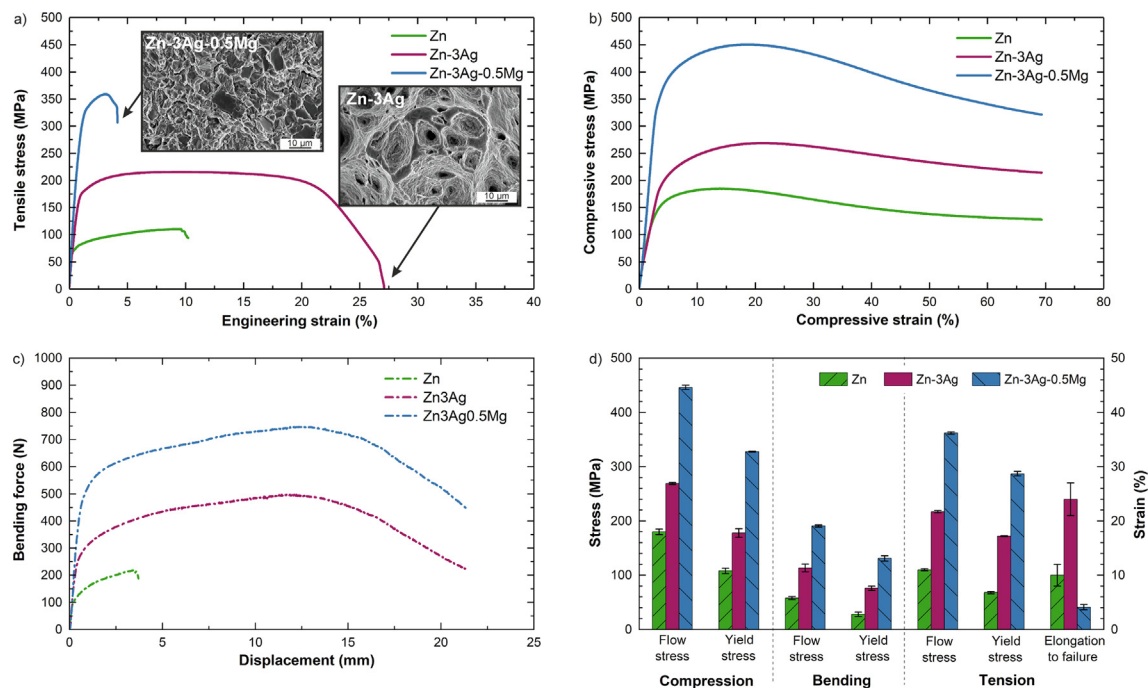


**Fig. 2.** Tensile (a), compression (b), bending curves (c) and summarized mechanical properties (d) of HE pure Zn, Zn-3Ag, and Zn-3Ag-0.5Mg alloys. Fractographic images in Fig. 2a present SEM morphology of the tensile fracture surface of Zn-3Ag and Zn-3Ag-0.5Mg alloys. Results in (d) are given as mean  $\pm$  standard deviation (\*\*\*)  $p < 0.001$ .

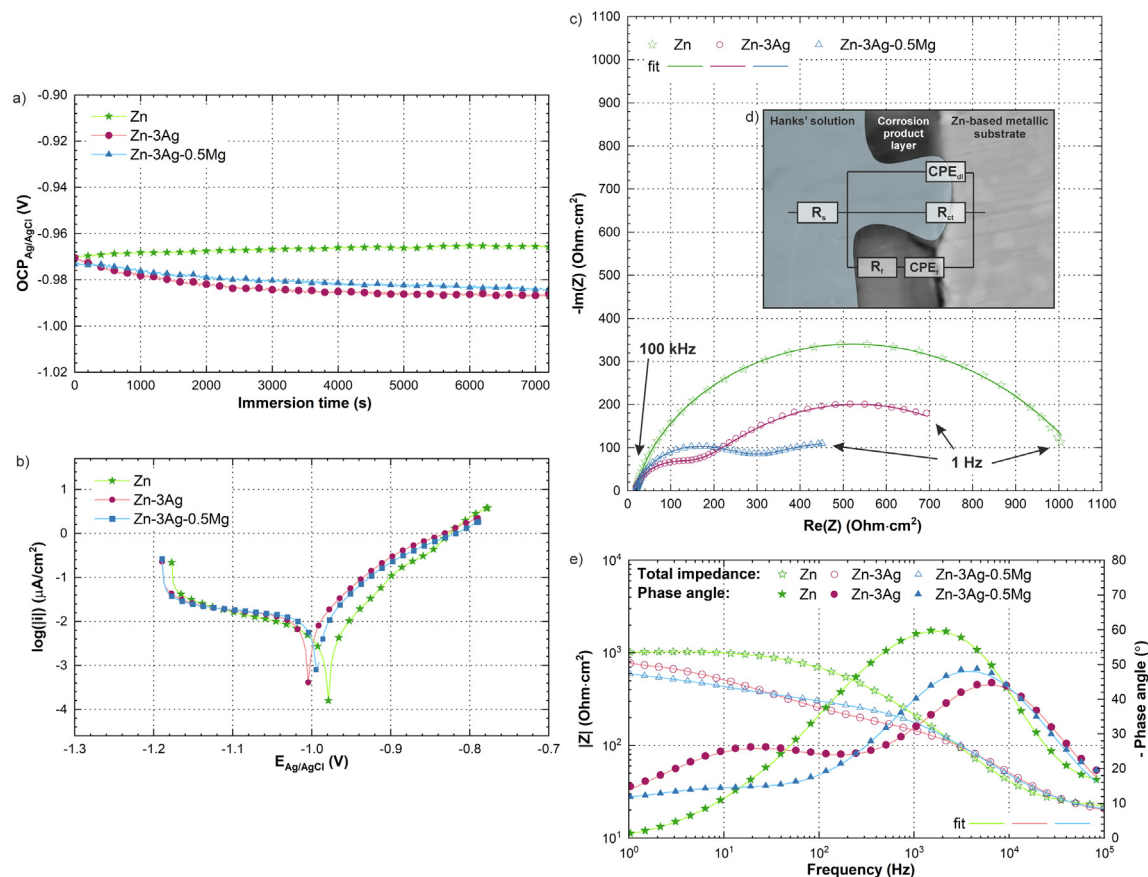


**Fig. 3.** Electrochemical measurements of the investigated samples: OCP (a), polarization curves (b), Nyquist plots (c), schematic representation of the used equivalent circuit model (d), and Bode plots (e).

descending order:  $-0.963$  V for pure Zn,  $-0.984$  V for the Zn-3Ag-0.5Mg alloy, and  $-0.986$  V for the Zn-3Ag alloy.

Representative polarization curves of the investigated materials are shown in Fig. 3b. The electrochemical parameters determined by Tafel extrapolation of the presented curves and calculated corrosion rates are summarized in Table 2. Electrochemical measurements performed in Hanks' solution show that the Zn-3Ag alloy demonstrates a more negative potential ( $-1.003$  V) compared to pure Zn ( $-0.978$  V), which indicates increased surface reactivity of the former. Simultaneously, Mg addition resulted in a corrosion potential ( $-0.988$  V) between pure Zn and the Zn-3Ag alloy. During potentiodynamic measurements, the scan was initiated from  $-200$  mV vs. the determined OCP, which may result in the partial reduction of oxides and other compounds present on the materials' surface. In turn, this would generate changes in the electrochemical properties of the corrosion products film/electrolyte interface. This effect would be directly responsible for the slight differences in OCP and  $E_{\text{corr}}$  values observed for particular materials. However, as the observed differences in OCP and  $E_{\text{corr}}$  values are subtle, this suggests similar corrosion properties of the analyzed materials. It should be noted that corrosion properties do not only depend on the materials' chemical composition, but also on other microstructural factors, including grain size, grain boundary density, as well as the presence of intermetallic precipitates.

The lowest corrosion current density, and thus, the slowest corrosion rate of  $135.3 \pm 14.2$   $\mu\text{m}/\text{year}$ , was recorded for pure Zn. Ag and Mg additions increased the corrosion current and accelerated the corrosion rate up to  $156.4 \pm 6.8$   $\mu\text{m}/\text{year}$  and  $188.2 \pm 17.5$   $\mu\text{m}/\text{year}$  for Zn-3Ag and Zn-3Ag-0.5Mg, respectively. Noticeably, all samples underwent surface passivation in the anodic range, when oxides and hydroxides start to form, and subsequently, the passive film grows. However, no plateau region is observed in the anodic branch, therefore determining the passivation current density was not possible. Furthermore, slight inflection can be detected in the cathodic range of the polarization curves. The inflection point may be attributed to the transition of the cathodic reaction from the activation to diffusion control range. Within the applied potential range, no changes in the Tafel curves in the anodic branch were observed, indicating corrosion product film breakdown and initiation of pitting corrosion at the so-called breakdown potential. Pitting corrosion takes place more willingly in the presence of  $\text{Cl}^-$  ions present in Hanks' solution and attack the defects present in the corrosion product film [36].

Fig. 3c and e present Nyquist and Bode phase and magnitude plots, respectively. The impedance data associated with the applied model circuit and fitted parameters are collected in Table 3. In the selected electrical equivalent circuit (EEC), Hanks' solution (electrolyte) resistance is characterized by  $R_s$ . The cathodic branch of equivalent circuit is represented by a constant phase element ( $\text{CPE}_f$ ) related to the corrosion product layer of a capacitance  $Q_f$ , while  $R_f$  refers to corrosion product film resistance. The anodic branch is characterized by a parallel circuit, composed of another  $\text{CPE}_{dl}$ , related to the double layer capacitance  $Q_{dl}$ , and charge-transfer resistance  $R_{ct}$  [37]. The application of the CPEs instead of capacitors in the EEC model provides optimal agreement between the simulated and experimental impedance data. The impedance of

CPE is a combination of properties associated with heterogeneity, roughness, pores, species adsorption (nonuniform potential and current distribution), and distributed surface reactivity [38]. The frequency-independent parameter  $n$  ( $0 < n < 1$ ) is introduced to describe such specimen imperfections. If  $n$  is close to 1, the used CPE can be treated as a perfect capacitor [39].

In the Bode phase angle plots of the Zn alloys, two phase maxima are observed, indicating that electrode processes are represented by two time constants. In the case of the Zn-3Ag-0.5Mg alloy, a maximum existing in the low frequency range is much less visible compared to the Zn-3Ag alloy. Maxima visible in the low frequency range are attributed to the protective layer formed at the alloys' surface, while those observed in the higher frequency range are attributed to the electrical double layer. In the case of pure Zn, only one phase maximum corresponding to the double layer is observed in the applied frequency range. It can be seen that the phase angle values in the low frequency range are consistent with  $Q_f$  and  $R_f$  values presented in Table 3. This indicates that the corrosion products formed on the surface of pure Zn are less stable than those forming on Zn alloys' surfaces. The total impedance magnitude value in the low frequency range indicates that, among the tested materials, pure Zn exhibits the highest corrosion resistance, which is consistent with  $C_R$  values determined based on potentiodynamic tests (Table 2).

Compared to pure Zn, higher  $R_{ct}$  values were recorded for the Zn alloys. This parameter is related to the rate of charge transfer on the metallic samples' surface. It is supposed that the higher potential of the Zn-based matrix grains enriched in Ag results from Ag limiting the dissolution process compared to the dissolution of pure Zn grains. However, the  $R_{ct}$  is lower in the ternary alloy compared to the binary one, which can result from the existence of Mg-rich intermetallic phases in the microstructure, promoting micro-galvanic corrosion-induced charge transfer processes [40–43]. The Zn-3Ag and Zn-3Ag-0.5Mg alloys' corrosion product films are more resistive than the one formed on pure Zn, as they are characterized by increased resistance  $R_f$  and increased capacitance  $Q_f$ . The highest value of  $R_f$  recorded for Zn-3Ag-0.5Mg alloy can be related to the formation of a thicker or intact corrosion layer retarding the overall corrosion reaction.

Surface morphology SEM observations (Fig. 4a–c) indicate a thin corrosion product film on the surface of samples with randomly distributed white spherical corrosion products on top. Corrosion product removal (Fig. 4d–f) revealed that pitting was one of the main corrosion mechanisms occurring during corrosion tests in Hanks' solution. In pure Zn, hexagonal-like pits have also been observed by Huang et al. [44]. In the Zn-3Ag and Zn-3Ag-0.5Mg alloys, the pits' dimensions are in the range of several micrometers and, in the ternary alloy, the pits had a similar size to the Mg-rich precipitates. The corroding Mg-rich precipitates were marked with yellow arrows in Fig. 4f, while the white  $\epsilon\text{-Zn}_3\text{Ag}$  precipitates do not seem to have been affected. This suggests that the  $\epsilon\text{-Zn}_3\text{Ag}$  phase exhibits a more electropositive stationary potential than the Mg-rich phase. This may, in turn, accelerate the dissolution of the Mg-rich phase due to the formation of local micro-galvanic cells. Furthermore, accumulation of electric field lines in preferred locations may be one of mechanisms responsible for the formation

**Table 2**

Electrochemical corrosion data and corrosion rate obtained from fitted results of polarization curves of the extruded samples in Hanks' solution.

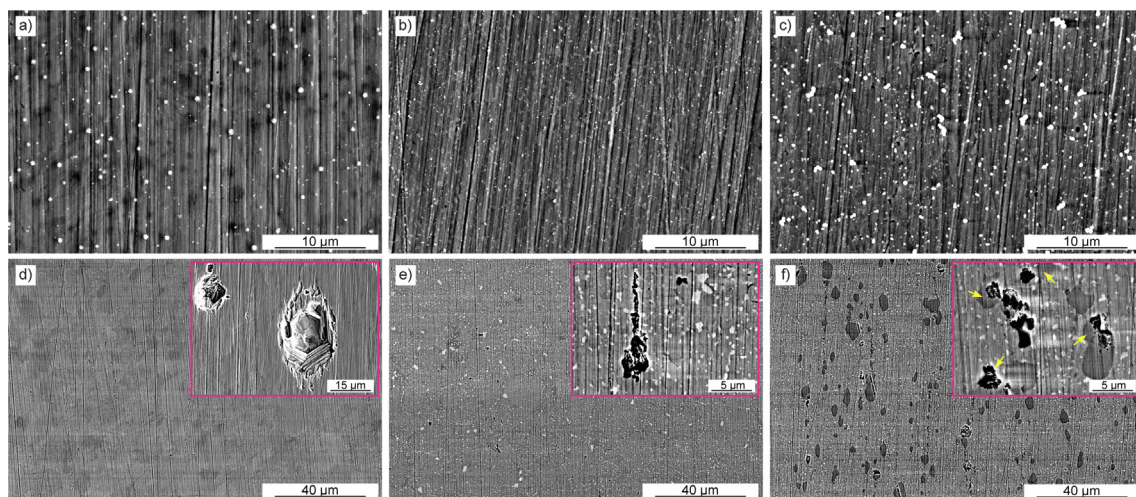
Sample	Corrosion potential, $E_{\text{corr}}$ (V) vs. Ag/AgCl	Current density, $i_{\text{corr}}$ ( $\mu\text{A}/\text{cm}^2$ )	Cathodic slope, $\beta_c$ (mV)	Anodic slope, $\beta_a$ (mV)	Corrosion rate, $C_R$ ( $\mu\text{m}/\text{year}$ )
Zn	$-0.978 \pm 0.003$	$7.8 \pm 2.0$	$262.9 \pm 19.9$	$72.6 \pm 6.7$	$135.3 \pm 14.2$
Zn-3Ag	$-1.003 \pm 0.002$	$10.6 \pm 0.5$	$439.4 \pm 7.8$	$75.0 \pm 1.9$	$156.4 \pm 6.8$
Zn-3Ag-0.5Mg	$-0.988 \pm 0.006$	$12.6 \pm 1.2$	$514.4 \pm 2.2$	$72.0 \pm 1.0$	$188.2 \pm 17.5$



**Table 3**

Fitted results of EIS spectra of the extruded samples. Please refer to the manuscript for the meaning of the symbols.

Sample	$R_s$ ( $\Omega \cdot \text{cm}^2$ )	$Q_f$ ( $\Omega^{-1} \cdot \text{cm}^{-2} \cdot \text{s}^{-1}$ )	$n_1$	$R_f$ ( $\Omega \cdot \text{cm}^2$ )	$Q_{dl}$ ( $\Omega^{-1} \cdot \text{cm}^{-2} \cdot \text{s}^{-1}$ )	$n_2$	$R_{ct}$ ( $\Omega \cdot \text{cm}^2$ )	$\chi^2$
Zn	11.18	$0.34 \cdot 10^{-6}$	0.99	20.46	$12.55 \cdot 10^{-6}$	0.61	417.5	0.003
Zn-3Ag	17.46	$0.10 \cdot 10^{-3}$	0.60	176.0	$1.98 \cdot 10^{-6}$	0.85	909.7	0.009
Zn-3Ag-0.5Mg	18.22	$0.19 \cdot 10^{-3}$	0.51	372.1	$2.83 \cdot 10^{-6}$	0.82	741.9	0.019

**Fig. 4.** Surface morphology after electrochemical corrosion tests (a-c) and after corrosion product layer removal (d-f) for pure Zn (a, d), and Zn-3Ag (b, e), Zn-3Ag-0.5Mg (c, f) alloys. Yellow arrows (f) indicate corroded Mg-rich precipitates.

of pits. Within the Zn-3Ag alloy, pits seem to form in a similar manner as in the Zn-3Ag-0.5Mg alloy. Here, the Ag-rich phase acts as a cathode, resulting in the privileged dissolution of more electronegative areas, and facilitating the appearance of pits (Fig. 4e) between Ag-rich areas.

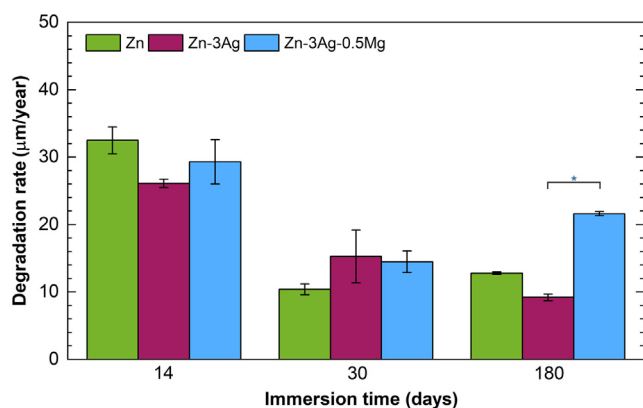
### 3.3. Immersion tests

The degradation rate of pure Zn and Zn alloys after 14, 30, and 180 days of Hanks' solution immersion tests are presented in Fig. 5. After 14 days, based on the calculated mass loss, pure Zn degraded at a rate of  $32.5 \pm 2.0$   $\mu\text{m}/\text{year}$ , while the Zn-3Ag and Zn-3Ag-0.5Mg alloys degraded at a slightly slower rate of  $26.1 \pm 0.6$   $\mu\text{m}/\text{year}$ , and  $29.3 \pm 3.3$   $\mu\text{m}/\text{year}$ , respectively. After 30 days of immersion, the degradation process slowed down to  $10.4 \pm 0.8$   $\mu\text{m}/\text{year}$ ,

$15.3 \pm 3.9$   $\mu\text{m}/\text{year}$ , and  $14.5 \pm 1.6$   $\mu\text{m}/\text{year}$  for pure Zn, Zn-3Ag, Zn-3Ag-0.5Mg, respectively. Prolonged immersion resulted in an ambiguous trend. Pure Zn demonstrated a similar corrosion rate as for 30 days ( $12.8 \pm 0.2$   $\mu\text{m}/\text{year}$ ), while the Zn-3Ag-0.5Mg alloy corroded almost twice as fast ( $21.8 \pm 0.3$   $\mu\text{m}/\text{year}$ ) as pure Zn, and interestingly, the corrosion of the Zn-3Ag alloy slowed down ( $12.8 \pm 0.2$   $\mu\text{m}/\text{year}$ ). It should be highlighted that a statistically significant difference between the samples at respective time points was noted only between Zn-3Ag-0.5Mg and Zn-3Ag alloys after 180 days.

The presented results are consistent with SEM microscopic observations. The morphology of the corrosion layer formed during immersion tests are presented in Fig. 6. As the immersion time increased, the amount of corrosion products on the specimens' surfaces gradually increased. After 30 days, all samples were entirely covered with a compact corrosion layer, on which uniformly distributed white globular clusters appeared (Fig. 6d-f). The cracks visible in the corrosion product films possibly result from internal stresses or dehydration during sample drying. The corrosion layer formed after 180 days was significantly thicker and more cracked. According to the EDS spectra collected from areas marked as "A" in Fig. 6j-l and results presented in Table 4 the thick corrosion layer is composed mainly of P, Ca, O. In the areas, where the corrosion product film peeled off, bare metal with a thin corrosive, marked as "B", mostly contained Zn and O, and only trace amounts of other elements can be observed. These areas were then exposed again directly to Hanks' solution, where further corrosive reactions could proceed.

According to the EDS analysis (Fig. 7), the corrosion layer in all samples was composed mainly of O, P, Ca, and Cl elements, whose concentration increased inversely to Zn with increasing immersion duration. Mg was mainly detected in the corrosion layer formed after prolonged immersion in Mg-containing Hanks' solution. The noticed presence of Mg in the case of pure Zn and Zn-3Ag alloy after 30-day immersion may result from near surface local pertur-

**Fig. 5.** Corrosion rate variation of the investigated samples immersed in Hanks' solution for 14, 30, and 180 days. All results are given as mean  $\pm$  standard deviation (\* $p < 0.05$ ).



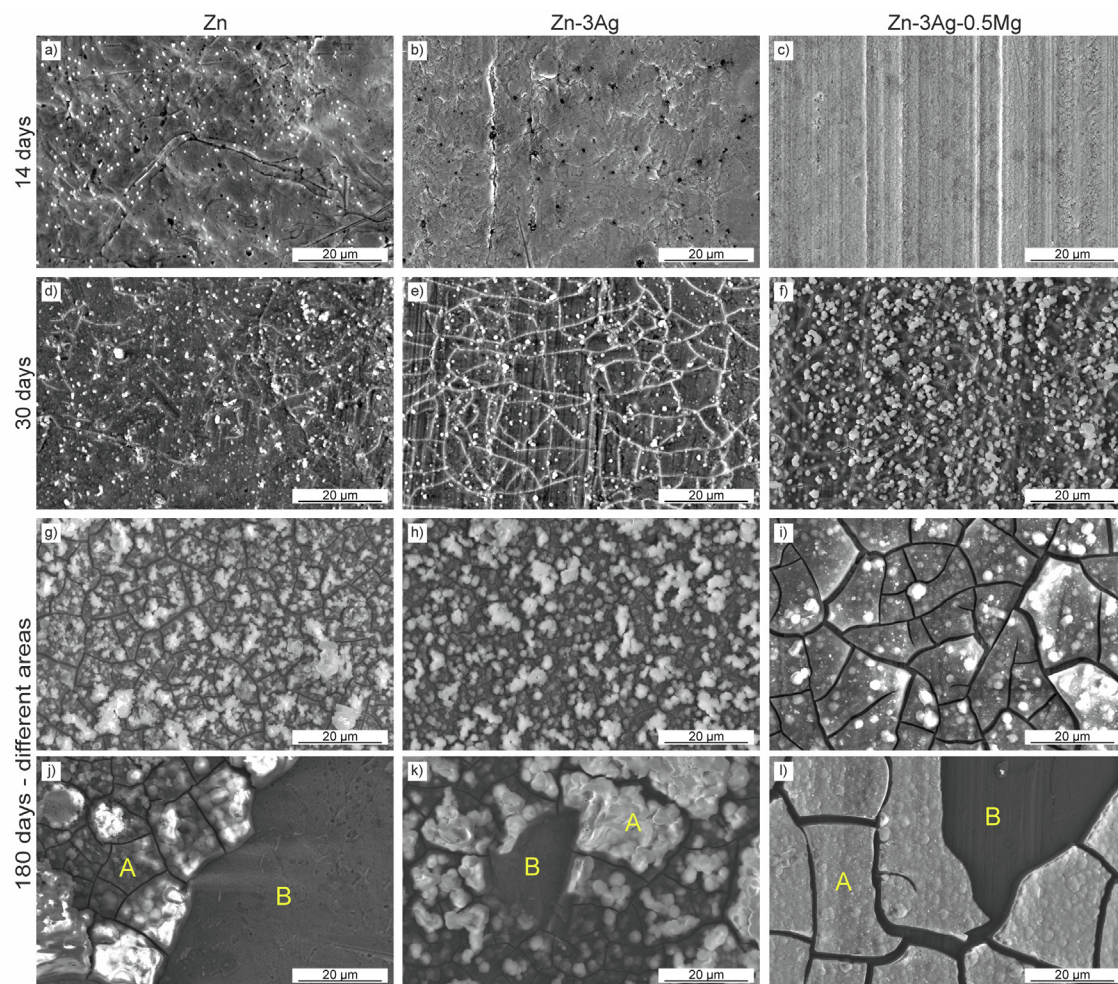


**Fig. 6.** Morphology of the corrosion layer formed after 14 days (a–c), 30 days (d–f), and 180 days (g–i) on the surface of pure Zn (a, d, g, j), Zn-3Ag (b, e, h, k), and Zn-3Ag-0.5Mg (c, f, i, l) alloys. A and B in Fig. j–l refer to the spots of EDS point analyses presented in Table 4.

**Table 4**

The atomic concentration of elements determined by EDS measurements in points A and B marked in Fig. 6j–l.

Sample	EDS point analysis	Atomic concentration (at.%) of elements						
		Zn	O	P	Ca	Cl	Mg	Ag
Pure Zn	point A	5.9	60.6	16.2	15.4	0.1	1.8	–
	point B	96.0	1.7	0.8	1.3	–	0.2	–
Zn-3Ag	point A	1.5	58.6	16.2	22.8	0.1	0.7	0.1
	point B	63.2	32.8	2.3	0.3	–	–	1.4
Zn-3Ag-0.5Mg	point A	2.4	70.2	12.0	13.9	0.1	1.3	0.1
	point B	59.5	32.2	2.1	–	–	4.7	1.5

bation of pH related to course of reactions responsible for material degradation which in turn providing proper conditions for Mg (OH)<sub>2</sub> precipitation [45]. A higher Mg concentration in the Zn-3Ag-0.5Mg corrosion layer after 14 days results from the presence of Mg in the alloy. The decreasing Zn and Ag concentrations may also be related to the increasing thickness of the corrosion product layer with increasing immersion duration, and less influenced by the signal contribution from the samples' base material during EDS analysis.

After careful degradation product removal, the samples' corroded surface morphologies were observed (Fig. 8). Pitting can be already observed after 14-day immersion on pure Zn and Zn alloys. The pits of a few micrometers size are uniformly distributed across

the samples' surface, however, occasionally some larger pits are also found (Fig. 8d). With increasing immersion time and complexity of the alloys' phase composition, the number of pits increases. In Fig. 8j–l, the images of magnified pits are presented. In the investigated Zn alloys, much finer features within the pits are visible. EDS point analysis indicated that bright grains (marked with pink crosses) are enriched in Ag. The Zn, Ag, O atomic concentrations averaged from several particles are 85.1 %, 13.0 %, 2.9 %, respectively, for the Zn-3Ag alloy, and 91%, 8.7%, 4.5%, respectively, for the Zn-3Ag-0.5Mg alloy. Collecting EDS spectra from the pits rather than from flat surface may affect the values in such a way that they do not fit ideally to the phase stoichiometry, however, the trends suggest that the bright particles belong to the ε-Zn<sub>3</sub>Ag phase. It



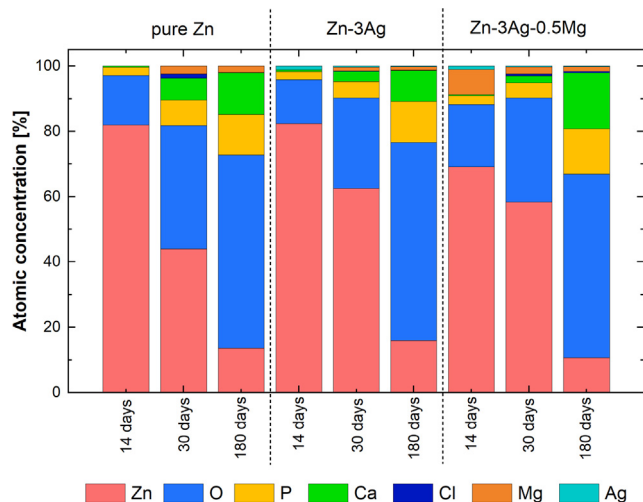


**Fig. 7.** The average elemental atomic composition of the corrosion products film formed on the investigated samples after different immersion times measured by EDS.

can be stated that no evident localized corrosion is observed after 180-day degradation testing that could result in catastrophic damage of the implant under working conditions.

### 3.4. Long-term degradation behavior: cross-sectional analysis and corrosion products identification

#### 3.4.1. SEM cross-section observations

There are many reports concerning the degradation behavior of Zn-based alloys immersed in physiological fluids for periods of up to 30 days [10,15], showing that regardless of the alloy's composition, the thin layer that first forms on top of Zn-based samples is composed mainly of primary corrosion products, like ZnO, Zn(OH)<sub>2</sub>, and Ca/P-based compounds [46–49]. This study extends upon these investigations by immersing samples in Hanks' solution for up to 180 days, providing details on the results of continued medium-material interactions. Fig. 9 shows the cross-sections of pure Zn, Zn-3Ag and Zn-3Ag-0.5Mg samples after 180-day immersion, which allow to follow the influence of the corrosion process on the integrity of the materials' structure. It can be seen that the degradation of pure Zn takes place uniformly via corrosion of whole grains (Fig. 9a). There are no signs of corrosion processes at the grain boundaries. In the Zn-3Ag alloy (Fig. 9b), intergranular corrosion can be observed. The inhomogeneous distribution of Ag within Zn grains, the depletion of Ag near the grain boundaries and the presence of  $\epsilon$ -Zn<sub>3</sub>Ag phase precipitates may result in privileged corrosion at the grain boundaries and nonuniform corrosion within the grains. The Ag-rich precipitates were not attacked and remain within the microstructure. In the refined multiphase microstructure of the Zn-3Ag-0.5Mg alloy (Fig. 9c) enriched in

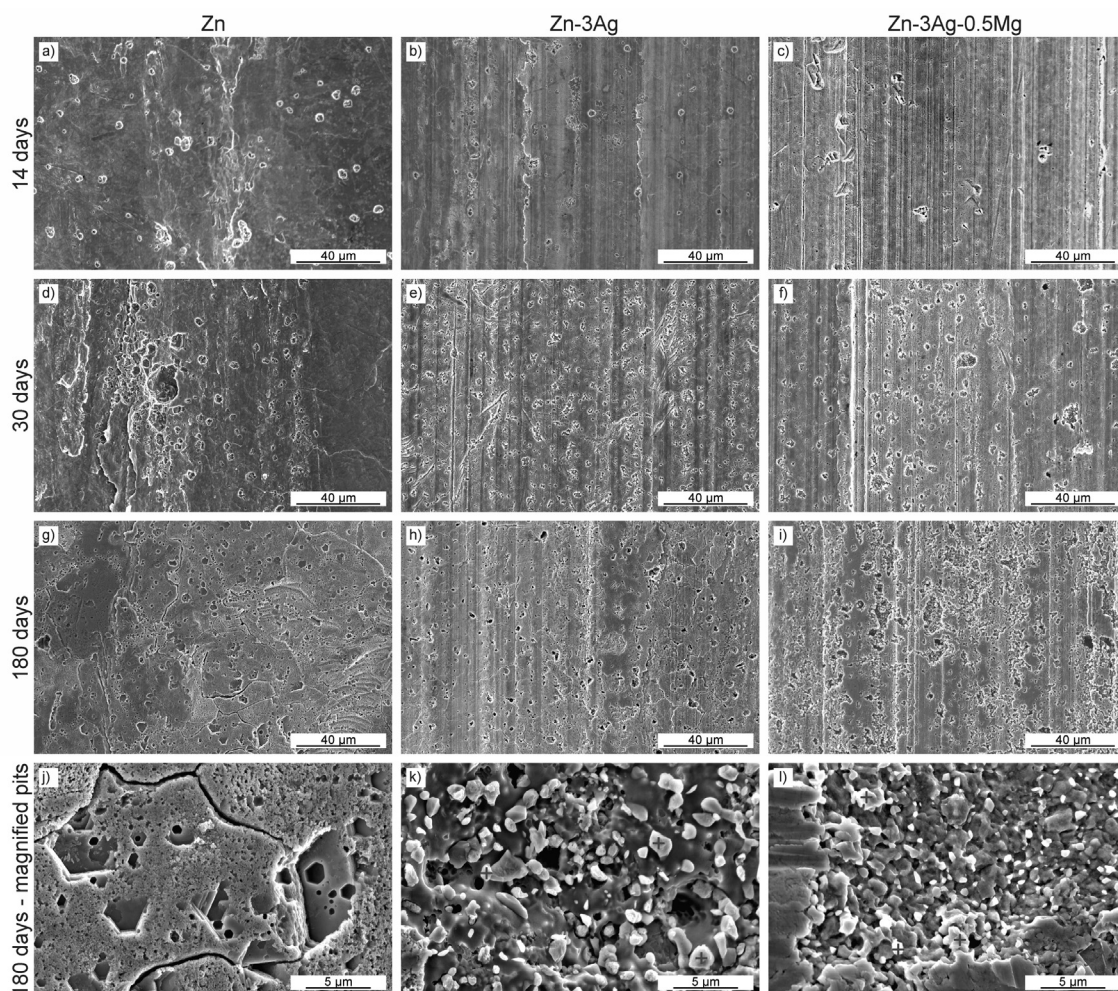


**Fig. 8.** Degraded surfaces after 14 days (a–c), 30 days (d–f), and 180 days (g–i) of the immersion tests and removing the corrosion layer from the samples: pure Zn (a, d, g), Zn-3Ag (b, e, h), Zn-3Ag-0.5Mg (c, f, i) alloys. Pink crosses (k, l) indicate Ag-rich precipitates remaining on the corroded surface.



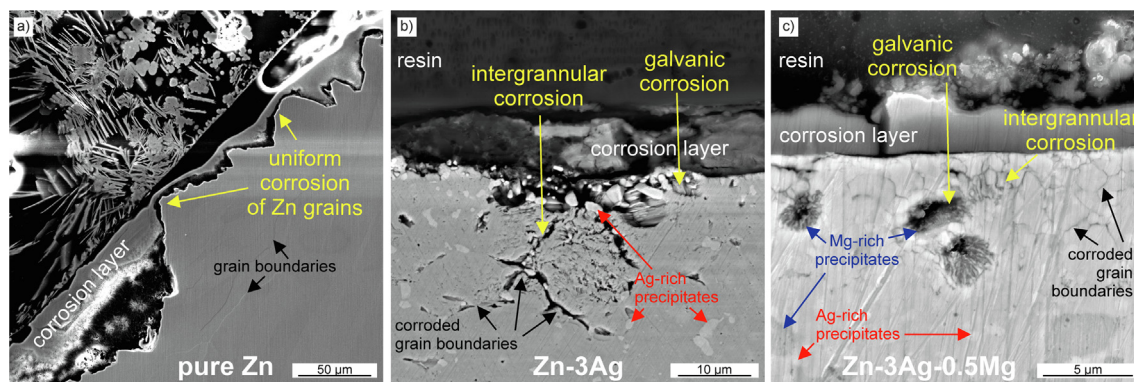


**Fig. 9.** Corrosion mechanisms shown on the cross-sections of pure Zn (a), Zn-3Ag (b), Zn-3Ag-0.5Mg (c) after 180 days of immersion in Hanks' solution.

the Mg-rich eutectic phase, there are clear signs of intergranular corrosion. The corrosion process began at the grain boundaries and developed within the Mg-rich precipitates. Like in Zn-3Ag, the  $\epsilon$ -Zn<sub>3</sub>Ag precipitates remained intact within the Zn-3Ag-0.5Mg alloy's microstructure.

While most of the samples' surfaces uniformly passivated and slowly corroded during the 180-day immersion test, much thicker corrosion layers formed in some regions, and the composition of the corrosion products changed. Fig. 10 shows the cross-sections and EDS maps of areas with relatively thin (approx. 3.5  $\mu$ m), compact, and homogeneous corrosion product layers (Fig. 10a-c), as well as more strongly attacked (10–50  $\mu$ m) areas (Fig. 10d-f). The corrosion product layers are marked with red arrows. The main elements found to occur in the corrosion product layer are O, P, Ca, and Mg, which is in good agreement with what was reported in Fig. 7. The distribution of C was omitted in the presented results, as the signal mainly comes from the epoxy resin. In Fig. 10a-c, only traces of Zn, most probably in the form of ZnO, are visible under the P- and Ca-based corrosion products. The regions that were more strongly affected by corrosion correspond to the larger pits observed after corrosion product removal in Fig. 8. The degradation in these areas occurred predominantly by localized corrosion and it is the primary source of the measured weight loss in the investi-

gated samples. Two different parts contribute to the developed corrosion layers. The inner corrosion products formed close to the substrates surface are mainly composed of Zn and O, with Zn being the product of substrate dissolution. The outer corrosion product layers, characterized by complex morphologies, are composed of P, Ca, O. It can be seen that the corrosion product layers of Zn and Zn-3Ag-0.5Mg are more porous than in the case of Zn-3Ag. A compact layer composed of Mg, Ca, P, O elements can inhibit corrosive medium penetration, limiting the dissolution of the Zn-based material beneath. This is in good agreement with the calculated slower degradation rate for the Zn-3Ag alloy compared to pure Zn and the Zn-3Ag-0.5Mg alloy described previously.

#### 3.4.2. Corrosion products identification

To identify the compounds in the observed corrosion layer, XRD was performed on pure Zn, Zn-3Ag, and Zn-3Ag-0.5Mg (Fig. 11). The XRD patterns resemble each other, with slight variations in the intensity of individual peaks. However, bearing in mind the complexity of collected XRD patterns, the proposed compounds should be treated as the most probable, and not the only possible ones. Apart from the peaks originating from the composition of the base metals, the main diffraction peaks are related to ZnO, Zn(OH)<sub>2</sub>, MgCO<sub>3</sub> and Zn<sub>5</sub>(OH)<sub>8</sub>Cl<sub>2</sub>·H<sub>2</sub>O. Zn<sub>3</sub>(PO<sub>4</sub>)<sub>2</sub>·4H<sub>2</sub>O compounds

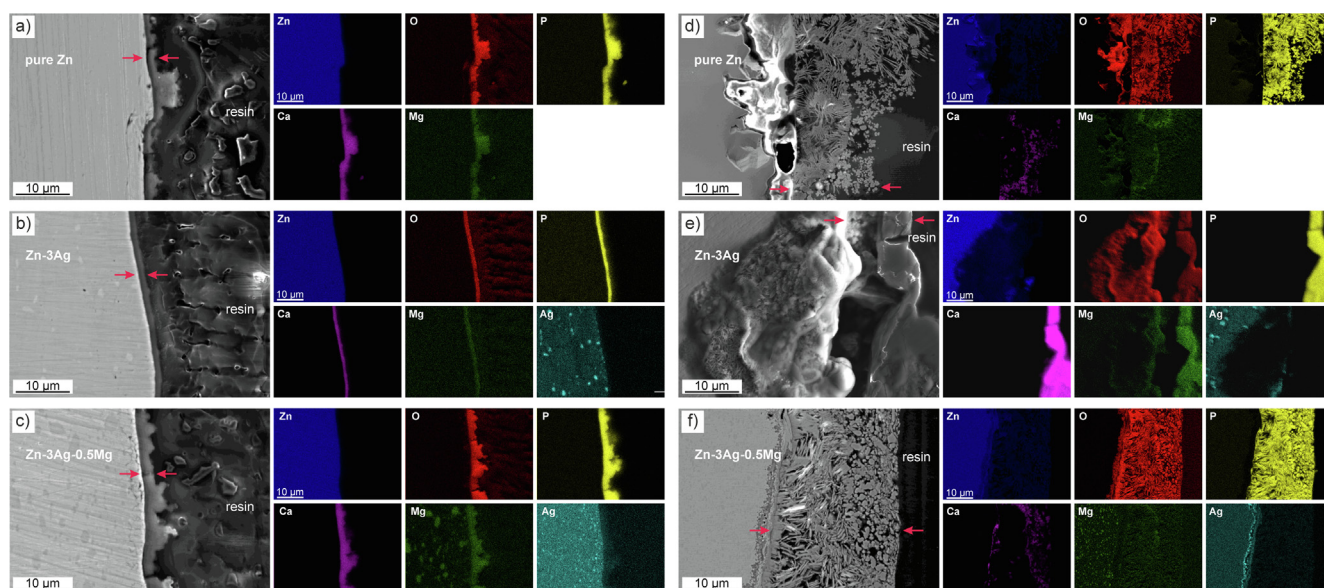


**Fig. 10.** EDS elemental distribution maps collected on the cross-sections of the corroded pure Zn (a, d), Zn-3Ag (b, e), Zn-3Ag-0.5Mg (c, f) after 180 days of immersion in Hanks' solution. Red arrows indicate the corrosion product layers: thin and compact (a-c), thicker and porous (d-f).



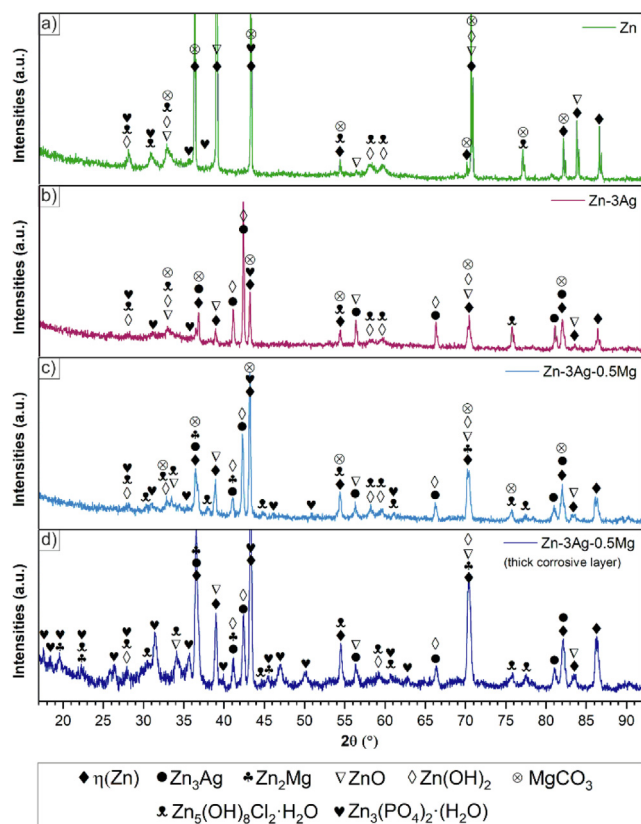


**Fig. 11.** XRD analysis of the corrosion products formed on pure Zn (a), Zn-3Ag (b), and Zn-3Ag-0.5Mg (c, d) after 180-day immersion in Hanks' solution.

were mainly detected in the thick corrosion layers (XRD presented on the example of the Zn-3Ag-0.5Mg alloy). In contrast to EDS results, Ca-containing compounds were not detected via XRD. However, it should not be excluded that Ca may substitute other elements in the identified corrosion products without changing the position of the peaks or can form compounds with too low intensities to be distinguished.

Further analysis of the corrosion products was performed via XPS (Fig. 12). The survey scan of all samples, shown in Fig. 12a, indicates no significant differences in chemical composition between the surfaces of the corroded samples. The identified peaks and calculated atomic concentrations of the elements shown in Fig. 12b reveal that the corrosion products are composed predominantly of C, O, Zn, Ca, P, with trace amounts of Na and Mg. To obtain more detailed information about the top layer of the corrosion products, high-resolution XPS data were additionally collected for Zn 2p<sub>3/2</sub> and Ca 2p. The main Zn 2p<sub>3/2</sub> spectra, centered at ~1022 eV for all samples, are shown in Fig. 12c. They present slightly asymmetrical features, which indicate the existence of other compounds included in these peaks. The Zn 2p<sub>3/2</sub> peaks were deconvoluted to two main components located at ~1023.7 eV and ~1021.7 eV. The first corresponds to Zn<sub>3</sub>(PO<sub>4</sub>)<sub>2</sub>·H<sub>2</sub>O, and the second peak centered at a lower bonding energy is attributed to ZnO/Zn(OH)<sub>2</sub> coexisted species. The contribution of Zn<sub>3</sub>(PO<sub>4</sub>)<sub>2</sub> in the Zn 2p<sub>3/2</sub> peak increased from 24.4 % for pure Zn to 31.1 % and 41.3 % for Zn-3Ag and Zn-3Ag-0.5Mg, respectively. The existence of Ca in the corrosion product layers was revealed in a narrow high-resolution XPS spectrum collected for Ca 2p. As demonstrated in Fig. 12d, the Ca 2p spectrum was fitted with two doublet structures. By analyzing the main 2p<sub>3/2</sub> deconvoluted peak bonding energies, it can be deduced that the peak's constituents are attributed to coexisting CaO/Ca(OH)<sub>2</sub> compounds

and Ca<sub>3</sub>(PO<sub>4</sub>)<sub>2</sub>. The Ca<sub>3</sub>(PO<sub>4</sub>)<sub>2</sub> compound contribution to the peak, analyzed in the 354 – 344 eV binding energy range, is 21.4 % for pure Zn and increased to 32.2 % for Zn-3Ag and 41.1 % for Zn-3Ag-0.5Mg. Knowing that in the XPS technique the signal is collected from a penetration depth not greater than a few atomic layers and much smaller than in EDS or XRD techniques, it is possible that Ca-based compounds are predominantly present in the outer corrosion product layer and can only be detected on the layers' surface.

## 4. Discussion

### 4.1. Effect of Ag and Mg additions on microstructure and deformation behavior

The materials' mechanical properties under tension, compression and bending were measured to determine their applicability as biomedical implants, which are subjected to load-bearing forces and different deformation modes. The obtained stress-strain (Fig. 2a, b) and stress-deformation (Fig. 2c) curves indicate that Ag and Mg additions significantly enhance both the yield stress and flow stress under all stress conditions, compared to pure Zn. The limited ductility of pure Zn is a result of its hexagonal close packed (HCP) crystal structure, while its low mechanical properties result from its low melting temperature (419.5 °C). The easiest dislocation slip is activated on basal and prismatic planes, while activation of pyramidal slips in Zn is not favored, due to the required high critical resolved shear stress value. Since the deformation by slip modes activated in Zn is not sufficient enough to satisfy the Von Mises criterion, deformation by twinning plays a fundamental role in accommodating plastic strain [50]. The differences in mechanical behavior observed during tension and compression are typical for hexagonal metals due to the deformation asymmetry related mainly to twinning polarity [51,52]. According to microstructures presented in the supplementary data (Fig. S1a,b), twinning was activated during tension of pure Zn, while under compressive force, dynamic recrystallization (DRX), resulting in significantly smaller, equiaxed grains being observed in the whole sample's volume.

The ability to accommodate plastic deformation in Zn is attributed to the grain size. In coarse-grained HCP materials, twinning is typically activated, while with increasing grain refinement, the contribution of dislocation slip and non-slip modes in total deformation increases [53]. The critical stress for twinning increases with decreasing grain size [54]. It is also possible to form shear bands during deformation in coarse-grained materials, where DRX can occur [55]. Twinning activation is correlated with the texture and loading direction. In contrast to Mg, in which the extension twins are observed during compression, the contraction {1 0 1̄ 2}>{1 0 1̄ 1̄}> twins are readily activated in Zn during tension [56,57]. In polycrystalline materials, twins nucleate mainly at grain boundaries (GBs), and under further straining, the twins propagate into the grains and typically end at an opposing grain boundary. However, the twin can propagate through the GBs and initiate at the next grain when straining is continued. It should be highlighted that deformation via twinning is limited, and this deformation mechanism is insufficient in accommodating the forced strain. The strengthening constant related to twinning is much higher than for dislocation slip, and when plastic strain cannot be further accommodated by the twinned grains, immediate fracture occurs [58,59]. Crack nucleation and propagation at twin boundaries, being high local stress concentration sites, is more likely to occur during tension than compression [53]. Stress-strain compressive curves, with visible decreasing stress recorded after reaching the maximum flow stress, indicate that DRX occurred

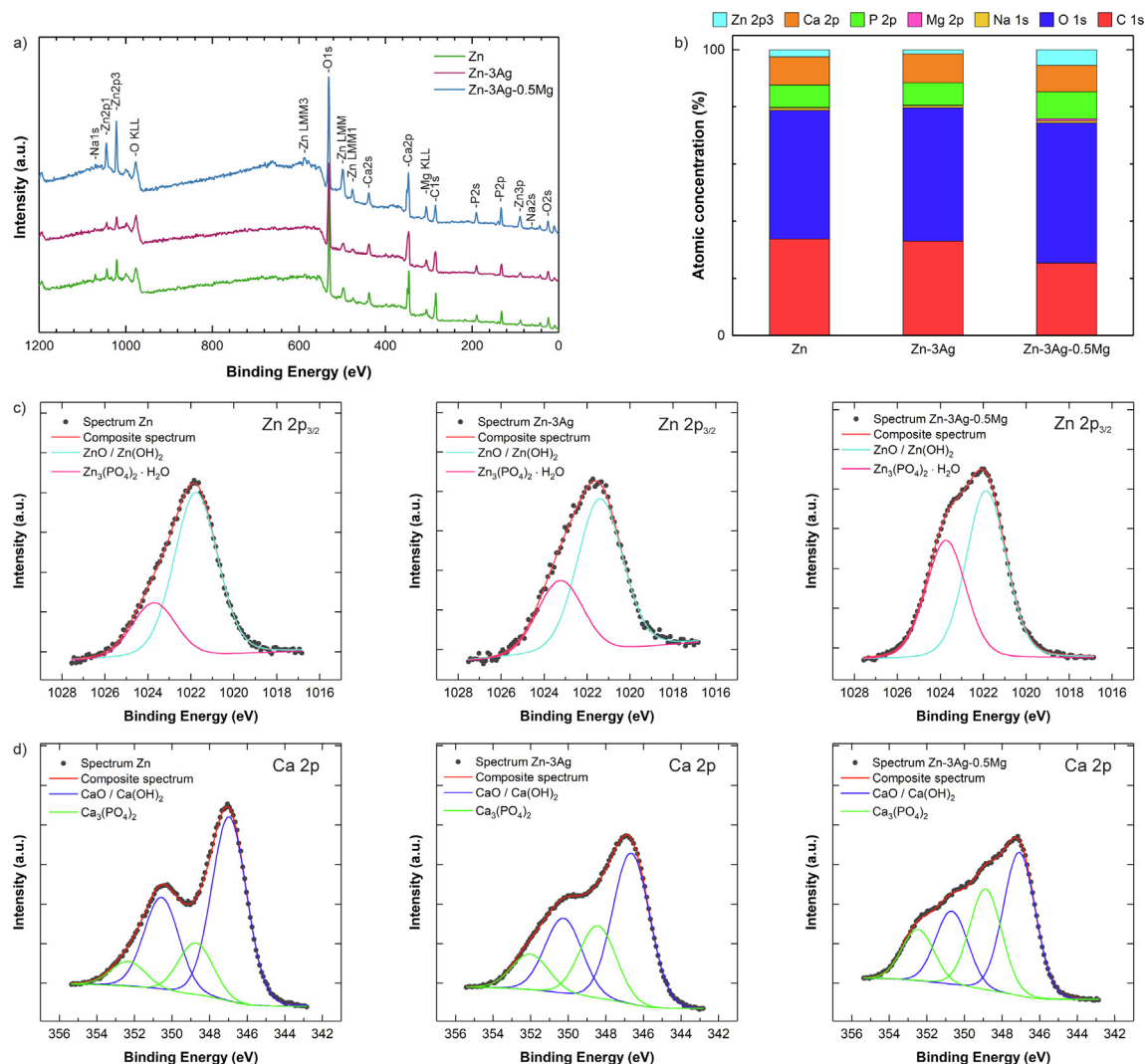


**Fig. 12.** XPS analysis of the corrosion layer formed on pure Zn, Zn-3Ag, and Zn-3Ag-0.5Mg after 180 days of immersion in Hanks' solution: XPS full spectra (a); average atomic concentration of elements occurring on the surface (b); XPS high-resolution narrow scan results for Zn 2p<sub>3/2</sub> (c) and Ca 2p (d).

during further deformation above 10 % of strain. It is supposed that twin boundaries can act as nucleation sites for DRX grains during compression, while in tension, they act as crack initiation sites [60]. Some microcracks have been observed at twin boundaries during compression of pure Zn, however, that was in the case of a much larger average grain size in the range of 3  $\mu\text{m}$  [61]. Three-point bending introduces both tensile and compressive stresses into the sample. It was shown in Fig. S1c,d that at the tension site of the bent sample, twinning occurred and was observed up to the neutral axis of the deformed sample, and DRX took place at the compression site. Thus, brittle fracture observed for Zn under bending resulted from twinning that cannot further accommodate the strain presented in the area of greatest deflection.

According to results presented in Fig. 1 and Figs. 2, 3 % of Ag refines the grain size, improves the strength, and increases ductility. The Zn-3Ag alloy presents the most extensive uniform deformation range during tension among the tested samples, after which an evident necking occurred, producing a ductile fracture mode. However, strengthening provided by the Ag addition is not sufficient to obtain the desired strength value for biodegradable implant material. According to [40], Zn-Ag alloys with higher Ag additions (up to 7 wt. %) demonstrated higher YS, UTS, and satisfactory plasticity. Besides grain refinement and solid solution

strengthening, Ag also contributes to the formation of the  $\epsilon$ -Zn<sub>3</sub>Ag precipitate. It has been reported that  $\epsilon$ -like peritectic precipitates and significant grain size refinement can lead to strain softening and activation of non-slip deformation mechanisms, e.g., grain/phase boundary sliding during deformation at room temperature (RT) [21,30,62,63]. Furthermore, the size of the formed  $\epsilon$ -Zn<sub>3</sub>Ag precipitates seems to be larger than the Zn matrix grains. These precipitates are additionally randomly distributed in the sample's volume and can be found inside the grains, however, due to their lack of ordering they do not provide effective strengthening, in contrast to Mg- or Li-rich phases in Zn alloys [17]. That is why the strong necking associated with localized deformation did not cause sudden fracture at low strains. Void nucleation and coalescence were observed in the deformed area mostly during tension (Fig. S1e). However, some small voids appeared at the tension site of bent samples, while grain shape and size indicate the occurrence of DRX in the compressed areas (Fig. S1f,h, Fig. S2a).

To address the insufficient strengthening effect of Ag and its  $\epsilon$ -Zn<sub>3</sub>Ag phase, the Mg addition was used to strengthen the grain boundaries within the fine-grained microstructure and limit deformation mechanisms, such as grain/phase boundary sliding [62]. Due to the relatively small grain size < 10  $\mu\text{m}$  in the Zn-3Ag-0.5Mg alloy, twinning may be suppressed to some extent in favor

of dislocation slip or non-slip deformation mechanisms [64]. Mg-rich precipitates and strengthened grain boundaries can act as barriers for dislocation movements or inhibit twinning expansion [65,66]. A narrow uniform deformation range was observed during the tension of the Zn-3Ag-0.5Mg alloy before fracture at ~5 % of total elongation. It should be emphasized that before fracture, some necking was also observed. The applied deformation mode provides a relatively large strain disproportionately concentrated in the necking area. Further straining is assisted by the nucleation of multiple voids within the hard, brittle Mg-rich precipitate bands present in the Zn-3Ag-0.5Mg alloy and visible in Fig S1i. They act as stress concentrators during straining, resulting in the fracture of weakened material via the formed voids [67].

The sudden fracture of the Zn-3Ag-0.5Mg alloy was not observed during compression and bending, where a wide range of plastic deformation was accommodated without visible cracks at the surface. During compression, as the applied strain induces more uniform deformation in the sample's volume, it contributes to the occurrence of DRX (Fig. S1j,l). Furthermore, shear bands or cleavage cracks did not occur due to the refined microstructure and relatively homogeneous distribution of second phases. During three-point bending, the highest local strain on the tension side must be smaller than the deformation in the neck during tension. As discovered for the dual-phase 1180 steel with continuous bending applied during tension, uniform depletion of ductility prevented localized strain concentration, resulting in increased elongation to fracture [68]. It can be seen in Fig. S2b that the voids nucleated at the tension site did not propagate into the neutral axis of the sample nor toward the sample's surface, but disappeared towards the compression site. The weakening of the tensile site did not result in fracture as the compressed and neutral center parts maintain sample integrity.

The Zn-3Ag-0.5Mg alloy after hot extrusion demonstrated the highest mechanical strength (UTS = 362 MPa, YS = 287 MPa), however, the ductility was not sufficiently high enough to fulfill the mechanical requirements for materials tested under tension conditions for use as biodegradable implants. Nevertheless, in our previous studies [27,30], it was presented that using additional cold deformation steps, such as severe plastic deformation or cold rolling inhibits the brittleness of high-strength Zn-based alloys without a significant drop in strength, resulting in the optimal combination of mechanical properties: UTS = 432 MPa, YS = 385 MPa,  $\epsilon_F$  = 34 %. This indicates a high potential of the Zn-3Ag-0.5Mg alloy to be considered as a biodegradable implant material.

#### 4.2. Corrosion mechanisms in Zn and Zn alloys

A series of chemical processes occur during the biodegradation process of Zn-based materials, when immersed in Hanks' solution that simulates the physiological fluids in a human organism after implantation. The most common corrosion modes for Zn alloy degradation are uniform corrosion, pitting corrosion, and galvanic corrosion, often associated with intergranular corrosion. The number of occurring (competing) corrosion mechanisms may increase with increasing Zn alloy chemical composition complexity.

It can be noticed that the corrosion process in pure Zn began predominantly at the GBs, as well as partially within the grains by creating shallow pores. The pit morphologies have a hexagonal crystallographic characteristic, confirming preferential attacks on particular crystal orientations with lower work functions. In Zn, the (0 0 0 1) basal plane is a close-packed plane attributed to a larger work function leading to higher corrosion resistance. These differences contribute to the formation of micro-galvanic couples between adjacent grains and higher electron transport at grain boundaries. Thus, their higher activity favors the dissolution of

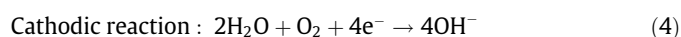
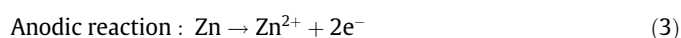
grain boundaries observed in pure Zn [7,44]. The standard electrode potential of the alloying elements in the examined materials is the following: 0.799 V for Ag, -0.762 V for Zn, and -2.372 V for Mg [69], and can affect the corrosion behavior of Zn alloys.

In the Zn-3Ag and Zn-3Ag-0.5Mg alloys, the  $Zn_3Ag$ ,  $Zn_{11}Mg_2$ / $Zn_2Mg$  precipitates affect the corrosion behavior in two ways. Firstly, Ag-rich or Mg-rich precipitates act as a cathodic or anodic site, respectively, during micro-galvanic corrosion with Zn-based matrix grains due to the difference in corrosion potential. In such a system, the anodic site dissolves faster. During 180-day immersion in Hanks' solution,  $\epsilon$ - $Zn_3Ag$  precipitates enrich the surface, which was confirmed by SEM-EDS analysis of the bright precipitates visible in Fig. 8k, l. Precipitates of the  $\epsilon$ - $Zn_3Ag$  phase act as cathodic sites in the micro-galvanic coupling with Zn-based matrix grains and remain undissolved within the analyzed immersion time range. Meanwhile, Mg-rich precipitates in the Zn-3Ag-0.5Mg alloy demonstrate a more electronegative potential, therefore they act as anodic sites and dissolve faster than adjacent Zn-based matrix grains [70]. Simultaneously, the dissolution of Zn-based matrix grains may occur more slowly. According to SEM observations, the Mg-rich grains are distributed uniformly in the alloy. For this reason the corrosion process initiates at many sites and corrosion gradually develops, resulting in the higher weight loss and accelerated degradation rate after 6 months of immersion in Hanks' solution. Micro-galvanic corrosion also accelerates the intergranular corrosion of Zn, especially when there are precipitates or some element enrichment or depletion in the grain boundary vicinity [41]. SEM images (Fig. 4f, 8) of the surface morphology after electrochemical experiments and corrosion product removal indicate that the dissolution is initiated within the Mg-rich grains and the pits tend to develop through the precipitates' entire volume. In contrast, the pit visible in Fig. 4e reveals more the dissolution of Zn-based matrix grains adjacent to the  $Zn_3Ag$  phase than the degradation of the precipitates. It is consistent with the corrosion process observed in the as-cast Zn-4Ag alloy [41], where the predominant dissolution of the Zn grains was noted.

The second type of observed corrosion behavior is related to the influence of phase presence on reducing the material's degradation rate. The phases form an effective physical barrier against progressive corrosion of the Zn matrix [71,72], especially when they are uniformly distributed throughout the microstructure. This partially explains why the degradation process in Zn-3Ag samples decreases with extended immersion duration. Additionally, as Ag is not only present in the precipitates but also forms a solid solution with Zn, the corrosion potential of the Zn-based matrix is shifted to a more anodic range compared to pure Zn, therefore the alloy exhibits decreased surface reactivity in the matrix area, which ultimately results in lower corrosion rates.

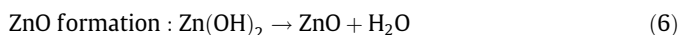
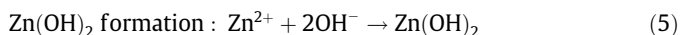
#### 4.3. Corrosion reactions

According to the Pourbaix diagram, Zn undergoes passivation in a neutral or alkaline environment [73]. However, when the corrosion product layer breaks down, the substrate material is penetrated by the solution through the formed cracks, allowing the corrosion process to continue. The process is more aggressive in the presence of  $Cl^-$  ions occurring in Hanks' solution [74]. Knowing that the degradation process of Zn in Hanks' solution occurs through anodic and cathodic reactions, leading to the formation of corrosion products identified based on SEM-EDS, XRD and XPS results, the biodegradation process can be described by the following reactions [12]:

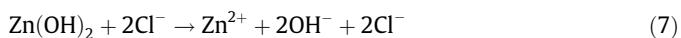




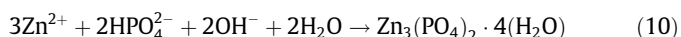
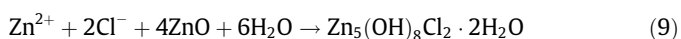
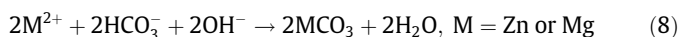
As a result of Zn dissolution, the pH of the solution increases, associated with a larger amount of  $\text{OH}^-$  ions present in the corrosive medium, leading to the formation of ZnO, according to reactions:



It is believed that ZnO is a more dominant and thermodynamically stable compound than  $\text{Zn(OH)}_2$  under physiological conditions. However,  $\text{Zn(OH)}_2$  can redissolve when in contact with  $\text{Cl}^-$ :



The presence of  $\text{HCO}_3^-$ ,  $\text{Cl}^-$ ,  $\text{HPO}_4^{2-}$  ions in Hanks' solution may be responsible for the formation of other phases along with the ZnO passive layer, such as zinc chloride hydroxide, zinc carbonate, or calcium phosphate. Other possible corrosion product formation reactions are the following:



The main advantage of Zn- over Mg-based materials is the absence of gas formation, especially hydrogen, during the degradation process in physiological fluids, as a high overpotential needs to be applied to Zn to induce the hydrogen evolution reaction.

According to Eq. (4), the reduction of  $\text{H}_2\text{O}$  leads to  $\text{OH}^-$  ions formation, shifting the solution's pH to the alkaline range. After electrochemical tests (Hanks' solution had primary pH of 7.4), the pH was  $7.61 \pm 0.02$ ,  $7.61 \pm 0.02$ ,  $7.63 \pm 0.04$  for pure Zn, Zn-3Ag, and Zn-3Ag-0.5Mg alloy, respectively. The change of pH was not significant due to the formation of  $\text{Zn(OH)}_2$  from the released  $\text{OH}^-$  ions and further transformation to ZnO and  $\text{H}_2\text{O}$  compounds. However, it can also be related to relatively low corrosion rates and, in turn, low ion release rates.

The composition of the corrosion products, mainly consisting of Zn, O, P, Ca and Mg, is similar for all investigated materials and is consistent with other reported results for *in vitro* corrosion of other alloy systems [11]. For instance, according to results presented for pure Zn immersed in simulated body fluid (SBF) (similar composition to Hanks' solution), the concentration of Zn in the corrosion layer decreases with immersion time in the presence of elements such as P, Ca, Mg, Cl detected in the corrosion product layer during chemical microanalysis what is in line with our observations [75]. In terms of long-term immersion in Hanks' solution, the composition of the corrosion product layer depends on its thickness. Based on the obtained results and available literature, the corrosion product layer consists of ZnO,  $\text{Zn(OH)}_2$ ,  $\text{Zn/Mg}(\text{CO}_3)_3$ ,  $\text{Zn}_5(\text{OH})_8\text{Cl}_2 \cdot \text{H}_2\text{O}$ ,  $\text{Zn}_3(\text{PO}_4)_2 \cdot 4\text{H}_2\text{O}$  that forms close to the substrate, while Ca-based compounds are found on the top of the corrosion products' surface. The effect of the corrosion products can be twofold, e.g., ZnO is known to accelerate the corrosion process due to the formation of the micro-galvanic cells with Zn, while Mg-based compounds,  $\text{Zn/Mg}(\text{CO}_3)_3$ , and  $\text{Zn}_5(\text{OH})_8\text{Cl}_2 \cdot \text{H}_2\text{O}$ , may inhibit the degradation process of the substrate.

#### 4.4. Biodegradation behavior and corrosion rate

The biodegradation behavior, including corrosion rate and corrosion product morphology, does not differ significantly between pure Zn and the investigated alloys. The only statistically meaningful difference was found between the two Zn alloys after 180 days of immersion, where Zn-3Ag degraded at half the rate of Zn-3Ag-

0.5Mg. The final corrosion rate will depend on the particular corrosion products ratio, medium pH, substrate microstructure, implantation site, and post-implantation period. For instance, the corrosion rate of a pure Zn implant in the femoral shaft was three times higher [76] than for the implant placed in the abdominal aorta [77]. This means that fabricated Zn alloy that corrodes at a rate  $\sim 20 \mu\text{m}/\text{year}$  under *in vitro* conditions should not be dedicated only to cardiovascular application and excluded from research as a potential material for bone-fixations, where the corrosion is required to be much faster,  $< 500 \mu\text{m}/\text{year}$ . As there are different factors influencing the material's final degradation rate, *in vitro* experiments should only be used as a tool to evaluate and compare the behavior of alloying elements under corrosive conditions against pure Zn.

When comparing the various literature reports concerning alloying addition effect vs corrosion rate for the selected Zn-Ag-Mg system, it is difficult to determine any clear trends or definitive correlations between chemical composition and biodegradation behavior. Considering the potential application of the investigated Zn-based materials and fundamental requirements for cardiovascular stents or fracture bone fixations, the results, including tensile strength vs. corrosion rate of certain materials, were gathered in Fig. 13. To reference results presented in current studies, only materials from the Zn-Ag-Mg system (binary and ternary alloys) after plastic deformation tested in a corrosive environment (*in vitro* or *in vivo*) for more than 7 days, were selected for the comparison. As can be seen, even small additions of Ag and/or Mg, combined with proper plastic deformation processing, significantly enhance the mechanical properties of Zn alloys. This shows that the investigated Zn-3Ag-0.5Mg alloy exhibits one of the highest tensile strengths among the referenced materials. Considering the same experimental conditions, neither Mg nor Ag additions drastically change the corrosion rate of Zn alloys compared to pure Zn. The differences between the results originating from various papers are more related to the experimental conditions, under which the biodegradation behavior of Zn alloys was studied, rather than alloying addition concentration. Therefore, it can be concluded that the biodegradation process of Zn-Mg alloys may be accelerated (lower wt. %) or slowed down (higher wt. %) depending on the Mg concentration, while Zn-Ag alloys seem to corrode faster with increasing Ag content. The corrosion rate in the Ag-enriched Zn alloys is below  $100 \mu\text{m}/\text{year}$  regardless of the Ag content up to 7 wt. %. The unambiguous effect of Mg may result from changing the relation between the corrosion product layer formation that inhibits the corrosion process, and micro-galvanic material dissolution that enhances corrosion development. It indicates that the investigated Zn-3Ag-0.5Mg alloy exhibits high potential for biodegradable stent applications. Nevertheless, it should be emphasized that *in vivo* conditions or dynamic flow of modified Hank's solution applied during *in vitro* testing can affect the calculated corrosion rate, therefore bone implant applications should not be excluded.

#### 4.5. Remaining corrosion products and selective dissolution of intermetallic phases

Corrosion products similar to the ones described in this study are likely to occur under *in vivo* conditions [34,77,85]. They have been reported to be safe for animal organs, not only for the adjacent local environment but also for other tissues. Additionally, Zn tested in a vascular environment exhibited the ability to produce absorbable corrosion products that do not accumulate excessively at the implantation site [77]. For biocompatibility, the released ions and formed degradation products should not induce local or systemic toxicity. Optimally, the released ions would support the remodeling or healing processes, for instance, as reported

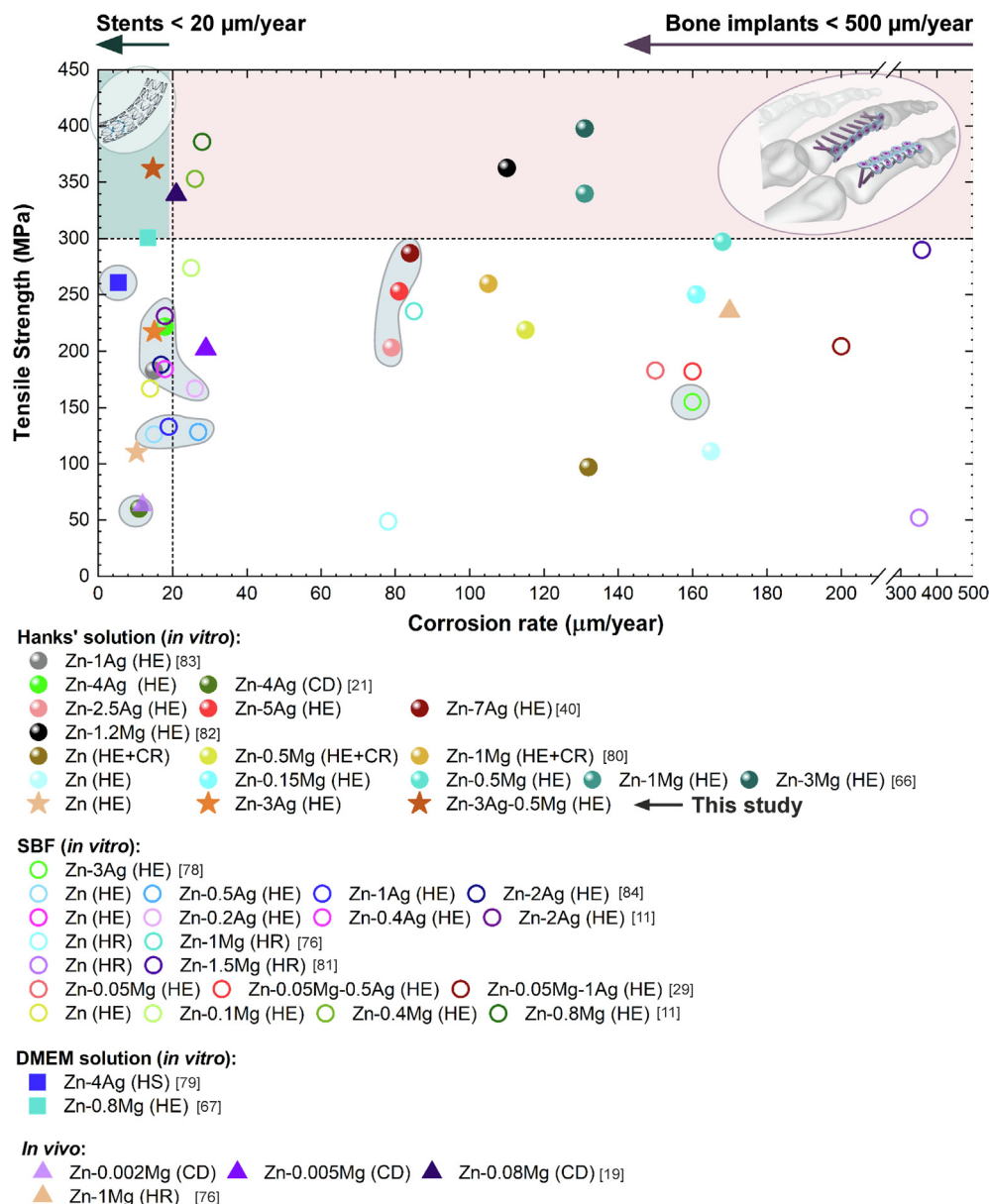


**Fig. 13.** Tensile stress vs. corrosion rate of selected materials from the Zn-Ag-Mg system. HE – hot extruded, HS – hot swagged, HR – hot rolled, CR – cold rolled, CD – cold drawn. The Zn-Ag binary alloys were additionally marked by grey areas. [11,19,21,29,40,66,67,76,78–84]

in the context of the neointimal smooth muscle cell hyperplasia suppression by activation of caspase-3-dependent apoptosis signaling pathways [86,87].

The presented degradation behavior (Fig. 9) involves two simultaneous mechanisms: 1) the dissolution of the Zn-based substrate through ion diffusion from Hanks' solution into the material, including intergranular and pitting corrosion, and 2) the formation of a corrosion product layer on the samples' surface, mainly composed of Zn-rich compounds, related to  $\text{Zn}^{2+}$  ion release. As visible in Fig. 9b, c, the grain boundaries act as highly reactive, easy-diffusion pathways that enhance ion transport to micro-galvanic matrix-precipitate sites. The main difference between the investigated samples is the morphology of the corrosion pits, which seem to be smaller and more uniformly distributed in the Zn alloys, especially in the Zn-3Ag-0.5Mg alloy, than in pure Zn. The difference in pit formation can result from the preferential dissolution of Mg-rich grains in Zn-3Ag-0.5Mg and the Zn-based matrix in pure Zn and Zn-3Ag. The only concern is related to the Ag content

and  $\epsilon\text{-Zn}_3\text{Ag}$  phase precipitates that corrode last, enriching the surface throughout the degradation progress. However, it has been reported that by applying cold plastic deformation followed by heat treatment results in the precipitation and dissolution the  $\text{Zn}_3\text{-Ag}$  phase [21]. This allows to control the corrosion rate of Zn-Ag-based alloys by the amount of Ag ions released from the degrading material. When more Ag is dissolved in the Zn-based solid solution, the anodic activity of the Zn-based matrix decreases, and the difference between the corrosion potential of the matrix and the second phase also decreases, so pitting corrosion caused by the galvanic coupling effect is reduced.

Moreover, the *in vivo* research reports no toxic effect of such small amounts of Ag in the Zn-xAg alloys ( $x = 0, 0.5, 1.0, 2.0$  wt. %), and relatively slow release of Ag-based degradation products or ions. Similar to our results, no Ag-based corrosion products were identified in the corrosion product layer, which may indicate that Ag is released in an ion form into the surrounding tissue [79]. The same research revealed that Zn-xAg alloys reduce the chance of

infection during degradation by releasing Zn and Ag ions around the implant into rat femoral bone. It's worth highlighting that the degradation products could effectively diffuse into the tissues adjacent to the implant site without affecting, or even promoting, osseointegration and inhibiting osteolysis. However, limited studies have been performed on the behavior of  $\epsilon$ -Zn<sub>3</sub>Ag precipitates during the degradation process should be performed, therefore further research is required to confirm the high potential of using Zn-Ag-based alloys for biodegradable applications.

## 5. Conclusions

In this work, the effect of Ag and Mg alloying additions on the microstructure, mechanical properties and corrosion behavior of Zn was investigated. Based on the performed analyses, the following conclusions can be put forward:

1. Ag additions significantly improve the strength and ductility in the Zn-3Ag alloy, based on the three tested deformation modes. Mg additions contribute to further strengthening and allow to fulfill biodegradable implant requirements, however, ductility deterioration during tension was observed. Under compressive and bending conditions, the narrow range of uniform deformation and brittle fracture of Zn-3Ag-0.5Mg alloy is no longer observed, confirming the deformation asymmetry in HCP metallic materials resulting additionally from lower amounts of localized strain under those stress states.
2. Biodegradation behavior studies reveal the corrosion product layer formation during immersion in Hanks' solution on the surface of the samples and report a decrease in degradation rate from  $29.3 \pm 4.7 \mu\text{m}$  (14 days) to  $14.8 \pm 2.7 \mu\text{m}$  (30 days). Ag and Mg additions in Zn alloys do not significantly affect the biodegradation rate calculated after 14 and 30 days. However, 6-month immersion caused degradation process acceleration in the case of pure Zn and Zn-3Ag-0.5Mg.
3. The main difference between the degrading materials is the dominant corrosion mode occurring during 180-day immersion in Hanks' solution. In pure Zn, the corrosion is relatively uniform, while the Ag and Mg additions result in intergranular and micro-galvanic corrosion, contributing to the formation of pits under the corrosion layer. It is related to 1) the change of electrochemical potential of the matrix grains by the dissolution of Ag in Zn, 2) the segregation of alloying additions towards grain boundaries and, in turn, inducing different electrochemical potentials at grain boundaries and inside the grains, and 3) the formation of micro-galvanic cells between the matrix Zn grains and intermetallic precipitates of Ag-rich and Mg-rich phases.
4. The presence of evenly distributed, small precipitates of second phases forming micro-galvanic couplings in the fine-grained microstructure with a high density of grain boundaries in the Zn-3Ag-0.5Mg alloy resulted in a uniform corrosion rate of  $21.8 \pm 0.4 \mu\text{m}$  without substantial localized corrosion after 180-day corrosion studies.

The presented results indicate that alloying can successfully address the limitation of pure Zn related to low strength and brittleness. The most relevant conclusion is that small additions of Mg and Ag, producing many intermetallic phase precipitates in the microstructure and changing the Zn matrix's electrochemical potential, do not lead localized corrosion and do not drastically affect the corrosion rate compared to pure Zn at the start of the degradation process. Following the requirements for biodegradable implant materials, the material should degrade at a rate allowing for the safe regeneration of the damaged tissue. When the tissue

is almost healed, the degradation process should accelerate to completely dissolve the implant in the human organism. The results indicate that the Zn-3Ag-0.5Mg alloy meets the necessary requirements. Nevertheless, the problem with the  $\epsilon$ -Zn<sub>3</sub>Ag precipitates remaining on the corroded surface requires further investigations and should be addressed in further research. Having in mind our previous mechanical studies [27,30], it means that the investigated Zn-3Ag-0.5Mg alloy exhibits promising properties for potential application as a biodegradable implant material. Low ductility, accompanied by high yield and tensile strength in the presented hot-extruded state, can be easily eliminated by further grain size refinement via cold deformation processes, e.g., cold rolling, drawing, or severe plastic deformation. The effect of the applied cold deformation, and subsequent grain size refinement, on the corrosion properties of the Zn-3Ag-0.5Mg alloy should also be taken under further consideration.

## Declaration of Competing Interest

The authors declare that they have no known competing financial interests or personal relationships that could have appeared to influence the work reported in this paper.

## Acknowledgments

This work was supported by the Polish National Science Centre [Grant number 2018/29/N/ST8/01703].

## Data availability

The raw/processed data required to reproduce these findings cannot be shared at this time as the data forms part of an ongoing study.

## Appendix A. Supplementary material

Supplementary data to this article can be found online at <https://doi.org/10.1016/j.matdes.2021.110289>.

## References

- [1] Y.F. Zheng, X.N. Gu, F. Witte, Biodegradable metals, *Mater. Sci. Eng. R Reports* 77 (2014) 1–34, <https://doi.org/10.1016/j.mser.2014.01.001>.
- [2] H.S. Han, S. Loffredo, I. Jun, J. Edwards, Y.C. Kim, H.K. Seok, F. Witte, D. Mantovani, S. Glyn-Jones, Current status and outlook on the clinical translation of biodegradable metals, *Mater. Today* 23 (2019) 57–71, <https://doi.org/10.1016/j.mattod.2018.05.018>.
- [3] E. Mostaed, M. Sikora-Jasinska, J.W. Drellich, M. Vedani, Zinc-based alloys for degradable vascular stent applications, *Acta Biomater.* 71 (2018) 1–23, <https://doi.org/10.1016/j.actbio.2018.03.005>.
- [4] D. Xia, F. Yang, Y. Zheng, Y. Liu, Y. Zhou, Research status of biodegradable metals designed for oral and maxillofacial applications: A review, *Bioact. Mater.* 6 (11) (2021) 4186–4208, <https://doi.org/10.1016/j.bioactmat.2021.01.011>.
- [5] A.A. Oliver, M. Sikora-Jasinska, A.G. Demir, R.J. Guillory, Recent advances and directions in the development of bioresorbable metallic cardiovascular stents: Insights from recent human and in vivo studies, *Acta Biomater.* 127 (2021) 1–23, <https://doi.org/10.1016/j.actbio.2021.03.058>.
- [6] Y. Liu, Y. Zheng, X.-H. Chen, J.-A. Yang, H. Pan, D. Chen, L. Wang, J. Zhang, D. Zhu, S. Wu, K.W.K. Yeung, R.-C. Zeng, Y. Han, S. Guan, Fundamental Theory of Biodegradable Metals—Definition, Criteria, and Design, *Adv. Funct. Mater.* 29 (18) (2019) 1805402, <https://doi.org/10.1002/adfm.201810022>.
- [7] B. Wei, D. Legut, S. Sun, H.T. Wang, Z.Z. Shi, H.J. Zhang, R.F. Zhang, Synergistic effect of solute and strain on the electrochemical degradation in representative Zn-based and Mg-based alloys, *Corros. Sci.* 188 (2021) 109539, <https://doi.org/10.1016/j.corsci.2021.109539>.
- [8] V. Hybasek, J. Kubasek, J. Capek, D. Alferi, J. Pinc, J. Jiru, J. Fojt, Influence of model environment complexity on corrosion mechanism of biodegradable zinc alloys, *Corros. Sci.* 187 (2021) 109520, <https://doi.org/10.1016/j.corsci.2021.109520>.



- [9] K. Chen, X. Gu, H. Sun, H. Tang, H. Yang, X. Gong, Y. Fan, Fluid-induced corrosion behavior of degradable zinc for stent application, *J. Mater. Sci. Technol.* 91 (2021) 134–147, <https://doi.org/10.1016/j.jmst.2021.02.050>.
- [10] H. Kabir, K. Munir, C. Wen, Y. Li, Recent research and progress of biodegradable zinc alloys and composites for biomedical applications: Biomechanical and biocorrosion perspectives, *Bioact. Mater.* 6 (3) (2021) 836–879, <https://doi.org/10.1016/j.bioactmat.2020.09.013>.
- [11] H. Yang, B. Jia, Z. Zhang, X. Qu, G. Li, W. Lin, D. Zhu, K. Dai, Y. Zheng, Alloying design of biodegradable zinc as promising bone implants for load-bearing applications, *Nat. Commun.* 11 (2020) 401, <https://doi.org/10.1038/s41467-019-14153-7>.
- [12] F. Rosalbino, G. Scavino, D. Macciò, A. Saccone, Influence of the alloying component on the corrosion behaviour of zinc in neutral aerated sodium chloride solution, *Corros. Sci.* 89 (2014) 286–294, <https://doi.org/10.1016/j.corsci.2014.09.007>.
- [13] G. Li, H. Yang, Y. Zheng, X.-H. Chen, J.-A. Yang, D. Zhu, L. Ruan, K. Takashima, Challenges in the use of zinc and its alloys as biodegradable metals: Perspective from biomechanical compatibility, *Acta Biomater.* 97 (2019) 23–45, <https://doi.org/10.1016/j.actbio.2019.07.038>.
- [14] D. Hernández-Escobar, Z.U. Rahman, H. Yilmazer, M. Kawasaki, C.J. Boehler, Microstructural evolution and intermetallic formation in Zn-Mg hybrids processed by High-Pressure Torsion, *Philos. Mag.* 99 (5) (2019) 557–584, <https://doi.org/10.1080/14786435.2018.1546962>.
- [15] J. Venezuela, M.S. Dargusch, The influence of alloying and fabrication techniques on the mechanical properties, biodegradability and biocompatibility of zinc: A comprehensive review, *Acta Biomater.* 87 (2019) 1–40, <https://doi.org/10.1016/j.actbio.2019.01.035>.
- [16] D. Hernández-Escobar, S. Champagne, H. Yilmazer, B. Dikici, C.J. Boehler, H. Hermawan, Current status and perspectives of zinc-based absorbable alloys for biomedical applications, *Acta Biomater.* 97 (2019) 1–22, <https://doi.org/10.1016/j.actbio.2019.07.034>.
- [17] Z.-Z. Shi, X.-X. Gao, H.-J. Zhang, X.-F. Liu, H.-Y. Li, C. Zhou, Y.-X. Yin, L.-N. Wang, Design biodegradable Zn alloys: Second phases and their significant influences on alloy properties, *Bioact. Mater.* 5 (2) (2020) 210–218, <https://doi.org/10.1016/j.bioactmat.2020.02.010>.
- [18] C. Chen, S. Fan, J. Niu, H. Huang, Z. Jin, L. Kong, D. Zhu, G. Yuan, Alloying design strategy for biodegradable zinc alloys based on first-principles study of solid solution strengthening, *Mater. Des.* 204 (2021) 109676, <https://doi.org/10.1016/j.matdes.2021.109676>.
- [19] H. Jin, S. Zhao, R. Guillory, P.K. Bowen, Z. Yin, A. Griebel, J. Schaffer, E.J. Earley, J. Goldman, J.W. Drelich, Novel high-strength, low-alloys Zn-Mg (< 0.1 wt% Mg) and their arterial biodegradation, *Mater. Sci. Eng. C* 84 (2018) 67–79, <https://doi.org/10.1016/j.msec.2017.11.021>.
- [20] M.S. Ardakani, E. Mostaed, M. Sikora-Jasinska, S.L. Kampe, J.W. Drelich, The effects of alloying with Cu and Mn and thermal treatments on the mechanical instability of Zn-0.05Mg alloy, *Mater. Sci. Eng. A* 770 (2020) 138529, <https://doi.org/10.1016/j.msea.2019.138529>.
- [21] E. Mostaed, M. Sikora-Jasinska, M.S. Ardakani, A. Mostaed, I.M. Reaney, J. Goldman, J.W. Drelich, Towards revealing key factors in mechanical instability of bioabsorbable Zn-based alloys for intended vascular stenting, *Acta Biomater.* 105 (2020) 319–335, <https://doi.org/10.1016/j.actbio.2020.01.028>.
- [22] Z. Li, Z.-Z. Shi, H.-J. Zhang, H.-F. Li, Y. Feng, L.-N. Wang, Hierarchical microstructure and two-stage corrosion behavior of a high-performance near-eutectic Zn-Li alloy, *J. Mater. Sci. Technol.* 80 (2021) 50–65, <https://doi.org/10.1016/j.jmst.2020.10.076>.
- [23] D. Lou, L. Wang, Y. Ren, H. Li, G. Qin, Textural evolution and improved ductility in Zn-0.2Mg-0.8Mn (wt%) alloys at different extrusion temperatures, *J. Alloys Compd.* 860 (2021) 158530, <https://doi.org/10.1016/j.jallcom.2020.158530>.
- [24] E. Farabi, J. Sharp, A. Vahid, J. Wang, D.M. Fabijanic, M.R. Barnett, S. Corujeira Gallo, Novel Biodegradable Zn Alloy with Exceptional Mechanical and In Vitro Corrosion Properties for Biomedical Applications, *ACS Biomater. Sci. Eng.* (2021), <https://doi.org/10.1021/acsbomaterials.1c00763>.
- [25] J. Sun, X. Zhang, Z.Z. Shi, X.X. Gao, H.Y. Li, F.Y. Zhao, J.Q. Wang, L.N. Wang, Development of a high-strength Zn-Mn-Mg alloy for ligament reconstruction fixation, *Acta Biomater.* 119 (2021) 485–498, <https://doi.org/10.1016/j.actbio.2020.10.032>.
- [26] P. Jiang, C. Blawert, M.L. Zheludkevich, The Corrosion Performance and Mechanical Properties of Mg-Zn Based Alloys—A Review, *Corros. Mater. Degrad.* 1 (2020) 7, <https://doi.org/10.3390/cmd1020007>.
- [27] M. Wątroba, W. Bednarczyk, J. Kawałko, S. Lech, K. Wiczerzak, T.G. Langdon, P. Bała, A Novel High-Strength Zn-3Ag-0.5Mg Alloy Processed by Hot Extrusion, Cold Rolling, or High-Pressure Torsion, *Metall. Mater. Trans. A* 51 (7) (2020) 3335–3348, <https://doi.org/10.1007/s11661-020-05797-y>.
- [28] A.L. Ramirez-Ledesma, P. Roncagliolo-Barrera, C. Paternoster, R. Casati, H. Lopez, M. Vedani, D. Mantovani, Microstructural Precipitation Evolution and In Vitro Degradation Behavior of a Novel Chill-Cast Zn-Based Absorbable Alloy for Medical Applications, *Metals (Basel)* 10 (2020) 586, <https://doi.org/10.3390/met10050586>.
- [29] C. Xiao, Y. Su, X. Zhu, W. Yu, D. Cui, X. Wei, X. Zhang, J. Li, F. Wang, Y. Ren, G. Qin, D. Zhao, Mechanical performance and biocompatibility assessment of Zn-0.05wt%Mg-(0.5, 1 wt%) Ag alloys, *J. Biomed. Mater. Res. Part B Appl. Biomater.* 108 (2020) 2925–2936, <https://doi.org/10.1002/jbm.b.34623>.
- [30] M. Wątroba, W. Bednarczyk, J. Kawałko, P. Bała, Fine-tuning of mechanical properties in a Zn-Ag-Mg alloy via cold plastic deformation process and post-deformation annealing, *Bioact. Mater.* 6 (10) (2021) 3424–3436, <https://doi.org/10.1016/j.bioactmat.2021.03.017>.
- [31] M.B. Kannan, H. Khakbaz, A. Yamamoto, Understanding the influence of HEPES buffer concentration on the biodegradation of pure magnesium: An electrochemical study, *Mater. Chem. Phys.* 197 (2017) 47–56, <https://doi.org/10.1016/j.matchemphys.2017.05.024>.
- [32] H. Baker (Ed.), *ASM Handbook: Alloy Phase Diagrams*, vol. 3, ASM International, 1998.
- [33] Y.N. Wang, J.C. Huang, Texture analysis in hexagonal materials, *Mater. Chem. Phys.* 81 (1) (2003) 11–26, [https://doi.org/10.1016/S0254-0584\(03\)00168-8](https://doi.org/10.1016/S0254-0584(03)00168-8).
- [34] P.K. Bowen, J. Drelich, J. Goldman, Zinc Exhibits Ideal Physiological Corrosion Behavior for Bioabsorbable Stents, *Adv. Mater.* 25 (18) (2013) 2577–2582, <https://doi.org/10.1002/adma.201300226>.
- [35] F. El-Taib Heakal, W.R. Abd-Ellatif, N.S. Tantawy, A.A. Taha, Impact of pH and temperature on the electrochemical and semiconducting properties of zinc in alkaline buffer media, *RSC Adv.* 8 (7) (2018) 3816–3827, <https://doi.org/10.1039/C7RA12723E>.
- [36] Y. Zhang, Y. Yan, X. Xu, Y. Lu, L. Chen, D. Li, Y. Dai, Y. Kang, K. Yu, Investigation on the microstructure, mechanical properties, in vitro degradation behavior and biocompatibility of newly developed Zn-0.8%Li-(Mg, Ag) alloys for guided bone regeneration, *Mater. Sci. Eng. C* 99 (2019) 1021–1034, <https://doi.org/10.1016/j.msec.2019.01.120>.
- [37] C.-C. Hung, W.-H. Lee, Y.-S. Wang, S.-C. Chang, Y.-L. Wang, Investigation of Galvanic Corrosion Between TaN x Barriers and Copper Seed by Electrochemical Impedance Spectroscopy, *Electrochem. Solid-State Lett.* 10 (2007) D100–D103.
- [38] Z. Cao, G. Kong, C. Che, Y. Wang, Influence of Nd addition on the corrosion behavior of Zn-5%Al alloy in 3.5wt.% NaCl solution, *Appl. Surf. Sci.* 426 (2017) 67–76, <https://doi.org/10.1016/j.apsusc.2017.07.109>.
- [39] J.-B. Jorcin, M.E. Orazem, N. Pébère, B. Tribollet, CPE analysis by local electrochemical impedance spectroscopy, *Electrochim. Acta* 51 (8–9) (2006) 1473–1479, <https://doi.org/10.1016/j.electacta.2005.02.128>.
- [40] M. Sikora-Jasinska, E. Mostaed, A. Mostaed, R. Beandlan, D. Mantovani, M. Vedani, Fabrication, mechanical properties and in vitro degradation behavior of newly developed Zn Ag alloys for degradable implant applications, *Mater. Sci. Eng. C* 77 (2017) 1170–1181, <https://doi.org/10.1016/j.msec.2017.04.023>.
- [41] K.B. Törne, F.A. Khan, A. Örnberg, J. Weissenrieder, Zn-Mg and Zn-Ag Degradation Mechanism Under Biologically Relevant Conditions, *Surf. Innov.* (2017) 1–41, <https://doi.org/10.1680/jsuin.17.00053>.
- [42] H. Gong, K. Wang, R. Strich, J.G. Zhou, In vitro biodegradation behavior, mechanical properties, and cytotoxicity of biodegradable Zn-Mg alloy, *J. Biomed. Mater. Res. Part B Appl. Biomater.* 103 (8) (2015) 1632–1640, <https://doi.org/10.1002/jbm.b.v103.810.1002/jbm.b.33341>.
- [43] P. Li, J. Qian, W. Zhang, C. Schille, E. Schweizer, A. Heiss, U.E. Klotz, L. Scheideler, G. Wan, J. Geis-Gerstörfer, Improved biodegradability of zinc and its alloys by sandblasting treatment, *Surf. Coatings Technol.* 405 (2021) 126678, <https://doi.org/10.1016/j.surfcoat.2020.126678>.
- [44] S. Huang, W. Wu, Y. Su, L. Qiao, Y. Yan, Insight into the corrosion behaviour and degradation mechanism of pure zinc in simulated body fluid, *Corros. Sci.* 178 (2021) 109071, <https://doi.org/10.1016/j.corsci.2020.109071>.
- [45] M. Kappes, M. Iannuzzi, R.M. Carranza, Hydrogen Embrittlement of Magnesium and Magnesium Alloys: A Review, *J. Electrochem. Soc.* 160 (4) (2013) C168–C178, <https://doi.org/10.1149/2.023304jes>.
- [46] H. Guo, J. Hu, Z. Shen, D. Du, Y. Zheng, J. Peng, In vitro and in vivo studies of biodegradable Zn-Li-Mn alloy staples designed for gastrointestinal anastomosis, *Acta Biomater.* 121 (2021) 713–723, <https://doi.org/10.1016/j.actbio.2020.12.017>.
- [47] J. Young, R.G. Reddy, Synthesis, mechanical properties, and in vitro corrosion behavior of biodegradable Zn-Li-Cu alloys, *J. Alloys Compd.* 844 (2020), <https://doi.org/10.1016/j.jallcom.2020.156257>.
- [48] P. Li, C. Schille, E. Schweizer, E. Kimmeler-Müller, F. Rupp, X. Han, A. Heiss, A. Richter, C. Legner, U.E. Klotz, J. Geis-Gerstörfer, L. Scheideler, Evaluation of a Zn-2Ag-1.8Au-0.2V Alloy for Absorbable Biocompatible Materials, *Materials (Basel)* 13 (2019) 56, <https://doi.org/10.3390/ma13010056>.
- [49] N. Yang, N. Balasubramani, J. Venezuela, S. Almathami, C. Wen, M. Dargusch, The influence of Ca and Cu additions on the microstructure, mechanical and degradation properties of Zn-Ca-Cu alloys for absorbable wound closure device applications, *Bioact. Mater.* 6 (5) (2021) 1436–1451, <https://doi.org/10.1016/j.bioactmat.2020.10.015>.
- [50] X. Liao, J. Wang, J. Nie, Y. Jiang, P. Wu, Deformation twinning in hexagonal materials, *MRS Bull.* 41 (4) (2016) 314–319, <https://doi.org/10.1557/mrs.2016.64>.
- [51] W. Bednarczyk, M. Wątroba, J. Kawałko, P. Bała, Determination of room-temperature superplastic asymmetry and anisotropy of Zn-0.8Ag alloy processed by ECAP, *Mater. Sci. Eng. A* 759 (2019) 55–58, <https://doi.org/10.1016/j.msea.2019.05.029>.
- [52] H. Watanabe, M. Fukusumi, Tension-Compression Asymmetry Under Superplastic Flow in Magnesium Alloys, *J. Mater. Eng. Perform.* 23 (10) (2014) 3551–3557, <https://doi.org/10.1007/s11665-014-1176-4>.
- [53] J.H. Liu, C.X. Huang, S.D. Wu, Z.F. Zhang, Tensile deformation and fracture behaviors of high purity polycrystalline zinc, *Mater. Sci. Eng. A* 490 (1–2) (2008) 117–125, <https://doi.org/10.1016/j.msea.2008.01.004>.
- [54] N. Ecob, B. Ralph, The effect of grain size on deformation twinning in a textured zinc alloy, *J. Mater. Sci.* 18 (8) (1983) 2419–2429, <https://doi.org/10.1007/BF00541848>.
- [55] J. Čapek, L. Kadeřávek, J. Pinc, J. Kopeček, L. Klimša, Influence of the Microstructure of the Initial Material on the Zn Wires Prepared by Direct

- Extrusion with a Huge Extrusion Ratio, *Metals* (Basel). 11 (2021) 787, <https://doi.org/10.3390/met11050787>.
- [56] T.B. Britton, F.P.E. Dunne, A.J. Wilkinson, On the mechanistic basis of deformation at the microscale in hexagonal close-packed metals Subject Areas, *Proc.R.Soc.A*. 471 (2178) (2015) 20140881, <https://doi.org/10.1098/rspa.2014.0881>.
- [57] M.H. Yoo, Slip, twinning, and fracture in hexagonal close-packed metals, *Metall. Trans. A*. 12 (3) (1981) 409–418, <https://doi.org/10.1007/BF02648537>.
- [58] M.A. Meyers, O. Vöhringer, V.A. Lubarda, The onset of twinning in metals: a constitutive description, *Acta Mater.* 49 (19) (2001) 4025–4039, [https://doi.org/10.1016/S1359-6454\(01\)00300-7](https://doi.org/10.1016/S1359-6454(01)00300-7).
- [59] D.J. Burr, N. Thompson, Twinning and fracture in zinc single crystals, *Philos. Mag.* 12 (116) (1965) 229–244, <https://doi.org/10.1080/14786436508218866>.
- [60] Y. Niu, Q. Le, F. Ning, J. Hou, Y. Jia, Strain induced dynamic recrystallization nucleation of ZA21 magnesium alloy during compression process at low and medium temperatures, *J. Mater. Res. Technol.* 9 (1) (2020) 340–346, <https://doi.org/10.1016/j.jmrt.2019.10.063>.
- [61] H. Li, Q.Q. Duan, X.W. Li, Z.F. Zhang, Compressive and fatigue damage behavior of commercially pure zinc, *Mater. Sci. Eng. A*. 466 (1–2) (2007) 38–46, <https://doi.org/10.1016/j.msea.2007.02.062>.
- [62] W. Bednarczyk, J. Kawałko, B. Rutkowski, M. Wątroba, N. Gao, M.J. Starink, P. Bała, T.G. Langdon, Abnormal grain growth in a Zn–0.8Ag alloy after processing by high-pressure torsion, *Acta Mater.* 207 (2021) 116667, <https://doi.org/10.1016/j.actamat.2021.116667>.
- [63] A. Jarzębska, Ł. Maj, M. Bieda, R. Chulist, D. Wojtas, M. Wątroba, K. Janus, Ł. Rogal, K. Sztwiertnia, Dynamic Recrystallization and Its Effect on Superior Plasticity of Cold-Rolled Bioabsorbable Zinc-Copper Alloys, *Materials* (Basel). 14 (2021) 3483, <https://doi.org/10.3390/ma14133483>.
- [64] W. Bednarczyk, M. Wątroba, J. Kawałko, P. Bała, Can zinc alloys be strengthened by grain refinement? A critical evaluation of the processing of low-alloyed binary zinc alloys using ECAP, *Mater. Sci. Eng. A*. 748 (2019) 357–366, <https://doi.org/10.1016/j.msea.2019.01.117>.
- [65] S. Liu, D. Kent, N. Doan, M. Dargusch, G. Wang, Effects of deformation twinning on the mechanical properties of biodegradable Zn–Mg alloys, *Bioact. Mater.* 4 (2019) 8–16, <https://doi.org/10.1016/j.bioactmat.2018.11.001>.
- [66] E. Mostaed, M. Sikora-Jasinska, A. Mostaed, S. Loffredo, A.G. Demir, B. Previtali, D. Mantovani, R. Beanland, M. Vedani, Novel Zn-based alloys for biodegradable stent applications: Design, development and in vitro degradation, *J. Mech. Behav. Biomed. Mater.* 60 (2016) 581–602, <https://doi.org/10.1016/j.jmbbm.2016.03.018>.
- [67] J. Kubásek, D. Vojtěch, E. Jablonská, I. Pospíšilová, J. Lipov, T. Ruml, Structure, mechanical characteristics and in vitro degradation, cytotoxicity, genotoxicity and mutagenicity of novel biodegradable Zn–Mg alloys, *Mater. Sci. Eng. C*. 58 (2016) 24–35, <https://doi.org/10.1016/j.msec.2015.08.015>.
- [68] C.M. Poulin, Y.P. Korkolis, B.L. Kinsey, M. Knezevic, Over five-times improved elongation-to-fracture of dual-phase 1180 steel by continuous-bending-under-tension, *Mater. Des.* 161 (2019) 95–105, <https://doi.org/10.1016/j.matdes.2018.11.022>.
- [69] P. Vanýsek, *Electrochemical series*, CRC Press LLC. (2008) 20–29.
- [70] J.M. Byun, J.M. Yu, D.K. Kim, T.-Y. Kim, W.-S. Jung, Y.D. Kim, Do Kim, Corrosion Behavior of Mg2Zn11 and MgZn2 Single Phases, *Korean J. Met. Materials*. 51 (6) (2013) 413–419, <https://doi.org/10.3365/KJMM.2013.51.6.413>.
- [71] X. Tong, D. Zhang, X. Zhang, Y. Su, Z. Shi, K. Wang, J. Lin, Y. Li, J. Lin, C. Wen, Microstructure, mechanical properties, biocompatibility, and in vitro corrosion and degradation behavior of a new Zn–5Ge alloy for biodegradable implant materials, *Acta Biomater.* 82 (2018) 197–204, <https://doi.org/10.1016/j.actbio.2018.10.015>.
- [72] Z.-Z. Shi, X.-X. Gao, H.-T. Chen, X.-F. Liu, A. Li, H.-J. Zhang, L.-N. Wang, Enhancement in mechanical and corrosion resistance properties of a biodegradable Zn–Fe alloy through second phase refinement, *Mater. Sci. Eng. C*. 116 (2020) 111197, <https://doi.org/10.1016/j.msec.2020.111197>.
- [73] P.K. Bowen, E.R. Shearier, S. Zhao, R.J. Guillory, F. Zhao, J. Goldman, J.W. Drelich, Biodegradable Metals for Cardiovascular Stents: from Clinical Concerns to Recent Zn-Alloys, *Adv. Healthc. Mater.* 5 (10) (2016) 1121–1140, <https://doi.org/10.1002/adhm.v5.1010.1002/adhm.201501019>.
- [74] K. Törne, M. Larsson, A. Norlin, J. Weissenrieder, Degradation of zinc in saline solutions, plasma, and whole blood, *J. Biomed. Mater. Res. Part B Appl. Biomater.* 104 (6) (2016) 1141–1151, <https://doi.org/10.1002/jbm.b.v104.610.1002/jbm.b.33458>.
- [75] L. Liu, Y. Meng, C. Dong, Y.u. Yan, A.A. Volinsky, L.-N. Wang, Initial formation of corrosion products on pure zinc in simulated body fluid, *J. Mater. Sci. Technol.* 34 (12) (2018) 2271–2282, <https://doi.org/10.1016/j.jmst.2018.05.005>.
- [76] H.F. Li, X.H. Xie, Y.F. Zheng, Y. Cong, F.Y. Zhou, K.J. Qiu, X. Wang, S.H. Chen, L. Huang, L. Tian, L. Qin, Development of biodegradable Zn–1X binary alloys with nutrient alloying elements Mg, Ca and Sr, *Sci. Rep.* 5 (2015) 10719, <https://doi.org/10.1038/srep10719>.
- [77] H. Yang, C. Wang, C. Liu, H. Chen, Y. Wu, J. Han, Z. Jia, W. Lin, D. Zhang, W. Li, W. Yuan, H. Guo, H. Li, G. Yang, D. Kong, D. Zhu, K. Takashima, L. Ruan, J. Nie, X. Li, Y. Zheng, Evolution of the degradation mechanism of pure zinc stent in the one-year study of rabbit abdominal aorta model, *Biomaterials*. 145 (2017) 92–105, <https://doi.org/10.1016/j.biomaterials.2017.08.022>.
- [78] M. Wątroba, W. Bednarczyk, J. Kawałko, K. Mech, M. Marciszko, G. Boelter, M. Banzhaf, P. Bała, Design of novel Zn–Ag–Zr alloy with enhanced strength as a potential biodegradable implant material, *Mater. Des.* 183 (2019) 108154, <https://doi.org/10.1016/j.matdes.2019.108154>.
- [79] X. Qu, H. Yang, B.o. Jia, M. Wang, B. Yue, Y. Zheng, K. Dai, Zinc alloy-based bone internal fixation screw with antibacterial and anti-osteolytic properties, *Bioact. Mater.* 6 (12) (2021) 4607–4624, <https://doi.org/10.1016/j.bioactmat.2021.05.023>.
- [80] C. Hehrlein, B. Schorch, N. Kress, A. Arab, C. von zur Mühlen, C. Bode, T. Epting, J. Haberstroh, L. Mey, H. Schwarzbach, R. Kinscherf, V. Stachniss, S. Schiestel, A. Kovacs, H. Fischer, E. Nennig, Zn-alloy provides a novel platform for mechanically stable bioresorbable vascular stents, *PLoS One*. 14 (2019) e0209111–1, <https://doi.org/10.1371/journal.pone.0209111>.
- [81] P. Li, C. Schille, E. Schweizer, F. Rupp, A. Heiss, C. Legner, U.E. Klotz, J. Geis-Gerstorfer, L. Scheideler, Mechanical characteristics, in vitro degradation, cytotoxicity, and antibacterial evaluation of Zn–4.0Ag alloy as a biodegradable material, *Int. J. Mol. Sci.* 19 (3) (2018) 755, <https://doi.org/10.3390/ijms19030755>.
- [82] S. García-Mintegui, L.C. Córdoba, J. Buxadera-Palomero, A. Marquina, E. Jiménez-Piqué, M.-P. Ginebra, J.L. Cortina, M. Pegueroles, Zn–Mg and Zn–Cu alloys for stenting applications: From nanoscale mechanical characterization to in vitro degradation and biocompatibility, *Bioact. Mater.* 6 (12) (2021) 4430–4446, <https://doi.org/10.1016/j.bioactmat.2021.04.015>.
- [83] D. Zhu, I. Cockerill, Y. Su, Z. Zhang, J. Fu, K.-W. Lee, J. Ma, C. Okpokwasili, L. Tang, Y. Zheng, Y.-X. Qin, Y. Wang, Mechanical Strength, Biodegradation, and in Vitro and in Vivo Biocompatibility of Zn Biomaterials, *ACS Appl. Mater. Interfaces*. 11 (7) (2019) 6809–6819, <https://doi.org/10.1021/acsami.8b20634.1021/acsami.8b20634.s001>.
- [84] C. Shen, X. Liu, B.o. Fan, P. Lan, F. Zhou, X. Li, H. Wang, X. Xiao, L. Li, S. Zhao, Z. Guo, Z. Pu, Y. Zheng, Mechanical properties, in vitro degradation behavior, hemocompatibility and cytotoxicity evaluation of Zn–1.2Mg alloy for biodegradable implants, *RSC Adv.* 6 (89) (2016) 86410–86419, <https://doi.org/10.1039/C6RA14300H>.
- [85] S. Zhao, J.-M. Seitz, R. Eifler, H.J. Maier, R.J. Guillory, E.J. Earley, A. Drelich, J. Goldman, J.W. Drelich, Zn–Li alloy after extrusion and drawing: Structural, mechanical characterization, and biodegradation in abdominal aorta of rat, *Mater. Sci. Eng. C*. 76 (2017) 301–312, <https://doi.org/10.1016/j.msec.2017.02.167>.
- [86] A.A. Oliver, R.J. Guillory, K.L. Flom, L.M. Morath, T.M. Kolesar, E. Mostaed, M. Sikora-Jasinska, J.W. Drelich, J. Goldman, Analysis of Vascular Inflammation against Bioresorbable Zn–Ag-Based Alloys, *ACS Appl. Bio Mater.* 3 (10) (2020) 6779–6789, <https://doi.org/10.1021/acsabm.0c00740>.
- [87] R.J. Guillory, T.M. Kolesar, A.A. Oliver, J.A. Bock, M.L. Bocks, J.W. Drelich, J. Goldman, Zn<sup>2+</sup>-dependent suppression of vascular smooth muscle intimal hyperplasia from biodegradable zinc implants, *Mater. Sci. Eng. C*. 111 (2020) 110826, <https://doi.org/10.1016/j.msec.2020.110826>.